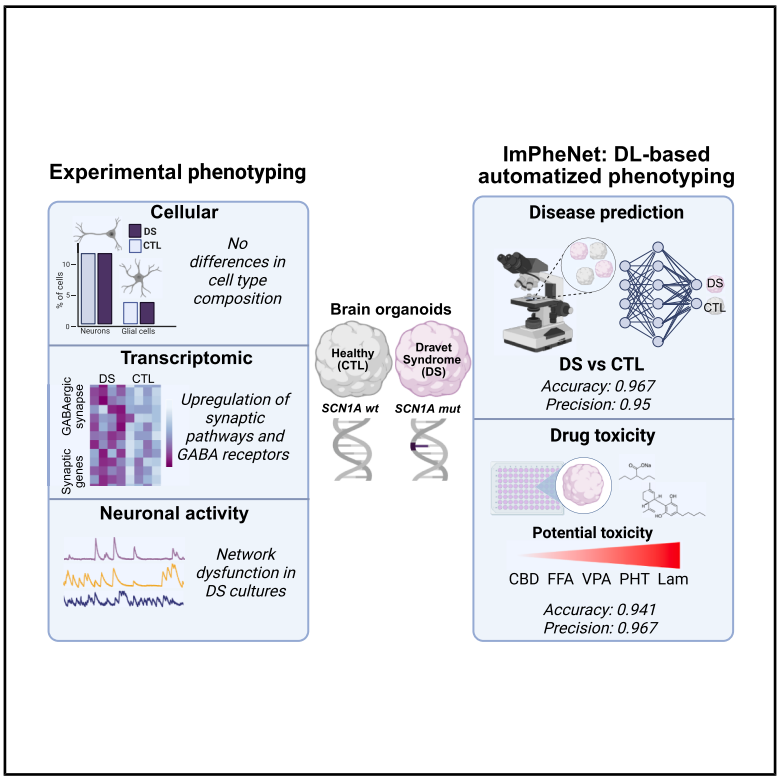
iScience

Article

Variability vs. phenotype: Multimodal analysis of Dravet syndrome brain organoids powered by deep learning

Graphical abstract



Highlights

- Dravet syndrome (DS) brain organoids show impaired network connectivity
- DS organoids' transcriptomic profile reveals an excitatory-inhibitory imbalance
- ImPheNet enables organoid phenotype classification despite morphological variability
- ImPheNet predicts anti-seizure drug toxicity in DS brain organoids

Authors

Isabel Turpin-Moreno, Adriana Modrego, Andrea Martí-Sarrias, ..., Daniel Tornero, Oscar Lao, Sandra Acosta

Correspondence

daniel.tornero@ub.edu (D.T.),
oscar.lao@upf.edu (O.L.),
sandra.acosta@ub.edu (S.A.)

In brief

Artificial intelligence; biological sciences; neuroscience; optical imaging; techniques in neuroscience

Turpin-Moreno et al., 2025, iScience *28*, 113831
November 21, 2025 © 2025 The Author(s). Published by Elsevier Inc.
https://doi.org/10.1016/j.isci.2025.113831

CellPress

iScience

CellPress
OPEN ACCESS

Article

Variability vs. phenotype: Multimodal analysis of Dravet syndrome brain organoids powered by deep learning

Isabel Turpin-Moreno,[1,2,3,16] Adriana Modrego,[1,2,16] Andrea Martí-Sarrias,[1,2,3] Laura García-González,[1,2,3] Alba Ortega-Gasco,[2,4,5] Anna-Christina Haeb,[2,4,5,6,7] Ruth Pareja,[1,2,3] Jordi Soriano,[6,7] Núria Ruiz,[1,8] Irene Peñuelas-Haro,[1,9] Elisa Espinet,[1,9] Arcadi Navarro,[3,10,11,12] Daniel Tornero,[2,4,5,13,*] Oscar Lao,[14,*] and Sandra Acosta[1,2,3,15,17,*]

[1]Department of Pathology and Experimental Therapeutics, Medical School, Universitat de Barcelona, Barcelona, Spain
[2]Institut of Neuroscience (INUB), Universitat de Barcelona, Barcelona, Spain
[3]Barcelona Brain Research Centre (BBRC), Barcelona, Spain
[4]Department of Biomedicine, Universitat de Barcelona, Barcelona, Spain
[5]August Pi i Sunyer Biomedical Research Institute (IDIBAPS), 08036 Barcelona, Spain
[6]Departament de Física de la Matèria Condensada, Universitat de Barcelona, Barcelona, Spain
[7]Universitat de Barcelona Institute of Complex Systems (UBICS), Barcelona, Spain
[8]Department of Pathology, Hospital Universitari de Bellvitge, L'Hospitalet de Llobregat, Barcelona, Spain
[9]Oncology Program, Institut d'Investigació Biomèdica de Bellvitge, L'Hospitalet de Llobregat, Barcelona, Spain
[10]Institució Catalana de Recerca i Estudis Avançats (ICREA) and Universitat Pompeu Fabra, Barcelona, Spain
[11]IBE, Institute of Evolutionary Biology (UPF-CSIC), Department of Medicine and Life Sciences, Universitat Pompeu Fabra, L'Hospitalet de Llobregat, Barcelona, Spain
[12]Centre for Genomic Regulation (CRG), The Barcelona Institute for Science and Technology, Barcelona, Spain
[13]Centro de Investigación Biomédica en Red Sobre Enfermedades Neurodegenerativas (CIBERNED), Madrid, Spain
[14]Group of Algorithms for Population Genomics, Department of Genetics, Institut de Biologia Evolutiva, IBE, (CSIC-Universitat Pompeu Fabra), Barcelona, Spain
[15]Neurocience Program, Institut de Recerca Sant Joan de Déu (IRSJD), Esplugues de Llobregat, Spain
[16]These authors contributed equally
[17]Lead contact
*Correspondence: daniel.tornero@ub.edu (D.T.), oscar.lao@upf.edu (O.L.), sandra.acosta@ub.edu (S.A.)
https://doi.org/10.1016/j.isci.2025.113831

SUMMARY

Dravet syndrome (DS) is a developmental epileptic encephalopathy (DEE) driven by pathogenic variants in the *SCN1A* gene. Brain organoids (BOs) have emerged as reliable models for neurodevelopmental genetic disorders, reproducing human brain developmental milestones and rising as a promising drug testing tool. Here, we determined the underlying molecular DS pathophysiology affecting neuronal connectivity, revealing an early onset excitatory-inhibitory imbalance in maturing DS organoid circuitry. However, neuronal circuitry modeling in BOs remains hampered by the notorious inter- and intra-organoid variability. Thus, leveraging deep learning (DL), we developed ImPheNet, a predictive tool grounded in BO live imaging datasets, to overcome the limitations of the intrinsic BOs variability. ImPheNet accurately classified healthy and DS phenotypes at early onset stages, revealing differences between genotypes and upon antiseizure drug exposure. Altogether, our DL-predictive live imaging strategy, ImPheNet, emerges as a powerful tool to accelerate DEEs research and advance toward treatment discovery in a time- and cost-efficient manner.

INTRODUCTION

The use of human brain organoids (BOs) has become a widespread tool to model neurodevelopmental disorders (NDDs) *in vitro*, due to their potential to reproduce in a simpler, more accessible, and inferable manner the physiological functions inherent in the human brain, both in healthy and pathological contexts. These advantages arise from the presence of reliable maturing neurodevelopmental 3D cellular structures growing in suspension, directly derived from human donors and/or patient-specific cells.[1–6] Despite being described more than a decade ago, organoids' widespread applicability has been hindered by two primary challenges: their predominantly immature phenotype and their intrinsic variability.[2,7] The inherent variability in BOs manifests at multiple levels: among organoids produced in the same batch, between experimental replicates (batches); and even more so, between different pluripotent stem cell (PSC) lines. Efforts to strike a balance between diversity and

This is an open access article under the CC BY-NC-ND license (http://creativecommons.org/licenses/by-nc-nd/4.0/).

reproducibility are essential for maximizing the potential of brain organoids as reliable and scalable models for studying human brain development and disease. For this purpose, various protocols for the generation of BOs have been proposed, broadly categorized into two approaches: guided and unguided. Guided organoids are more reproducible but show reduced cellular diversity.[3,4] Unguided BOs are characterized by high cellular diversity, better recapitulation of the layered cortical plate, but strong variability between organoids, even intraexperimentally.[8–11] The successful identification of phenotypic traits in BOs strongly relies on selecting the appropriate protocol, carefully balancing its advantages and disadvantages. In unguided protocols, two key stages contribute to the observed variability: the early neural induction and the establishment of the neuronal networks.[12–14] During early developmental stages, variability can lead to the stochastic generation of multiple regionalized areas and suboptimal cerebral organoids,[12,15] enriched with non-neural cell types and aberrant morphological traits. The origin and relevance of variability arising at later stages, when the conformation and the extension of the neuronal circuitry and its functional connectivity are being established, remain largely unexplored. It is associated with the generation of multiple neuronal subtypes, driven by cell-autonomous and non-cell autonomous mechanisms, and the heterochronic maturation of the multiple neurogenic rosettes.[3,12,16] Moreover, it remains unknown to what extent these inherent differences affect them at maturer stages, casting doubt on the use of BOs in late-onset disease modeling. By addressing these challenges, BOs can be harnessed to enhance our understanding of complex neurological processes and pave the way for novel therapeutic approaches.

Developmental and epileptic encephalopathies (DEEs) encompass a group of disorders characterized by frequent intractable seizures, brain developmental and functional defects, cognitive deficits, and, in some cases, premature mortality.[17] Dravet Syndrome (DS), the most common DEE, is associated with heterozygous pathogenic variants in the *SCN1A* gene, which encodes one subunit of the Nav1.1 voltage-gated sodium channel essential for the function of inhibitory neurons in the brain.[18,19] The epileptic phenotype in DS is caused by an imbalance in excitatory-inhibitory circuitry as a result of decreased sodium current in inhibitory neurons.[20,21] Other severe DEEs have been successfully modeled using brain organoids, such as Rett Syndrome, where epileptogenic currents were observed compared to isogenic cell lines.[22] In this context, the complexity and uniqueness of cerebral organoids analyzed through conventional molecular and histological techniques face significant challenges in identifying non-obvious phenotypes. Thus, leveraging Artificial Intelligence (AI)-based analyses of whole organoids emerges as a potential solution to overcome the intrinsic variability associated with human BOs during phenotyping approaches. AI has appeared as a transformative force in various fields, and its application in life sciences has revolutionized the way we approach research, diagnosis, and treatment.[23,24] Machine learning and deep learning (DL) algorithms have shown tremendous potential in handling vast amounts of complex biological data and extracting valuable insights. In life sciences, AI-driven approaches are being used to analyze genomics, transcriptomics, proteomics, and other high-throughput data, enabling researchers to identify patterns, biomarkers, and novel therapeutic targets.[25] Datasets derived from BO analysis leverage AI to integrate complex experimental information, enabling tasks such as growth tracking and phenotypic feature identification. Additionally, AI has proven its efficacy in predicting drug interactions, designing personalized treatment plans, and even discovering alternative drug candidates.[26] By merging advanced computational methods with biological knowledge, AI is accelerating scientific discovery and paving the way for more precise and personalized approaches to address various health challenges.

In this study, we model DS using BOs and uncover an underlying epilepsy-associated phenotype in their abnormal neuronal connectivity. Subsequently, we apply DL algorithms to quantify the potential of BOs to define the pathological phenotype using live-microscopy images. The multimodal analysis allows for discrimination between inherent BOs variability and genotype-associated phenotype. Using this approach, we determine that the phenotype rises above the intra- and inter-organoid variability and predict the potential toxic impact of anti-seizure drugs in DS. Altogether, we define the DS phenotype in BOs, and we propose a robust methodology based on live imaging and DL to boost the applications of BOs in translational biomedicine and therapeutic discovery.

RESULTS

Temporal and regional variability in human brain organoids

Unguided BO differentiation follows the ‘‘inside-out’’ pattern of cortical differentiation, similarly to human cerebral cortex development, where neurons are generated at the ventricular zone and then migrate outwards to form distinct layers. This process is heterochronic in BOs, and maturation rates differ among the regional structures. Here, we aim to monitor the maturation rates using live imaging in BOs. To follow maturation changes, human embryonic stem cells (hESCs) H9-derived BOs were stained at multiple stages (day 35-progenitor expansion and neurogenesis onset, day 60-neurogenesis, and day 90-maturing neuronal network and astrogenesis) with Cellbrite, a membrane dye with reduced toxicity (Figure 1A). This staining resolved organoid surface morphology and neural cytoarchitecture more accurately than brightfield (Figures 1A–1D and S1A–S1C; Video S1). Moreover, Cellbrite highlights the surface topography variability and the morphological differences among multiple organoids, and, remarkably among the multiple regional levels in the same organoid (Figures 1C and 1D). Cellbrite co-staining indicated its labeling specificity for immature and mature neurons (MAP2, TUBB3), including GABAergic interneurons (GAD65), and astrocytes (GFAP) in 90-day-old BOs (Figures S1D–S1H). In contrast, limited Cellbrite labeling was detected in 35-day-old BOs co-stained with Nestin (Figure S1H). Moreover, the neural cytoarchitecture at day 90 BOs analyzed 1 week after Cellbrite staining was conserved, as intermingled populations of neurons (NFM) and astrocytes (GFAP) appeared (Figure 1E), altogether supporting the use of Cellbrite as a suitable live imaging staining for longitudinal panneural network studies. At the cellular level, the maturation stage at day 90 of differentiation in H9 BOs exhibits

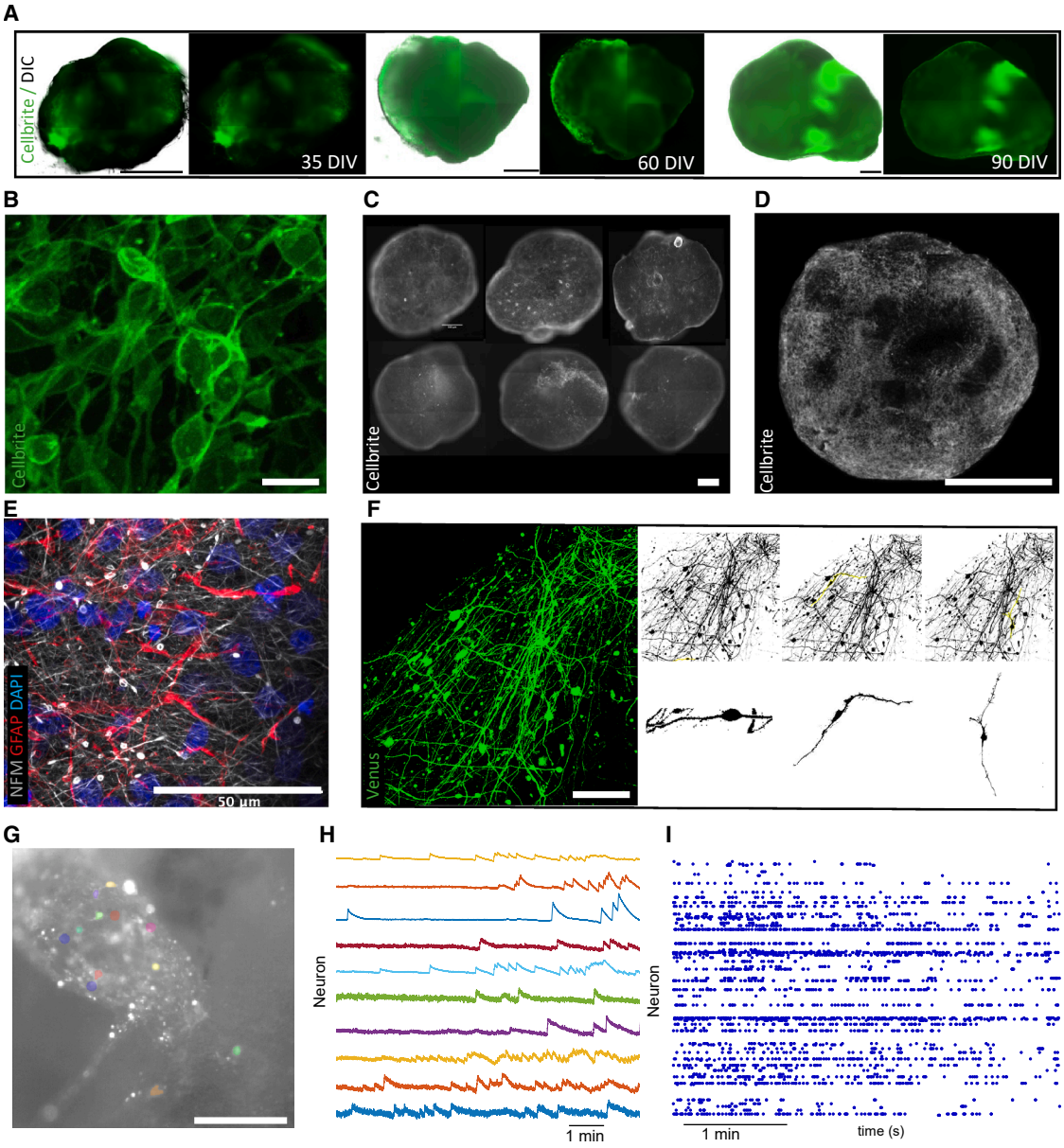


Figure 1. Morphological and functional reconstruction of intra-organoid variability

(A) Merged brightfield and Cellbrite fluorescent images from H9 brain organoids at days 35, 60, and 90 of differentiation, captured using an Axio Observer Z1 Apotome inverted fluorescent microscope. Scale bar: 500 µm. DIV: days *in vitro*.

(B) Live imaging of a 90-day-old brain organoid stained with Cellbrite. Image obtained using Confocal Carl Zeiss LSM 880 at 25x magnification. Scale bar: 20 µm.

(C) Inter-organoid variability of H9 brain organoids at day 90 of differentiation, stained with Cellbrite, captured using Axio Observer Z1 Apotome inverted fluorescent microscope. Scale bar: 250 µm.

(D) Whole-organoid maximal projection reconstruction of a high-magnification image of a fixed 90-day-old brain organoid stained with Cellbrite, obtained using Confocal Carl Zeiss LSM 880. Scale bar: 700 µm.

(E) Immunofluorescence (IF) staining of NFM and GFAP markers indicating the presence of mature neurons and astrocytes, respectively. Image deconvolution was performed with Airyscan2 inverted confocal microscope-associated software. Scale bar: 50 µm.

(F) Live-imaging (left) and single neuron segmentation (right) of low-dosage infection with a lentiviral Venus reporter on a 90-day-old brain organoid, showing heterogeneity in cell morphology and distribution across the surface.

(G) Fluorescent image of a GCaMP6s AAV infected day 90 brain organoid, indicating ROIs of active neurons. Scale bar: 400 µm.

(H) Calcium imaging activity traces of individual Syn1^{+} neurons from a 90-day-old brain organoid infected with GCaMP6s AAV.

(I) Raster plot shows firing the activity of individual Syn1^{+} neurons over 5 min.

a well-developed neuronal network with axonal terminations that connect multiple regions within the organoid (Figures 1B–1F and S1J), highlighting the morphological subregional variability.

Bulk transcriptomic analysis at multiple differentiation stages (days 21, 35, and 90) confirmed that, by day 90, organoids acquire an advanced maturing stage and differ significantly from day 21 and 35 brain organoids, which show an immature neural identity (Figures S2A–S2D). Genes involved in neuronal differentiation, maturation, and connectivity signatures change over time, suggesting temporal maturation in multiple stages. Early progenitor signature genes such as *SOX2*, *NES,* and *ASPM* were detected more strongly at earlier stages, whilst genes indicating mature neuronal signature, such as *SYN1*, *MAP2*, *DLG4* (PSD-95), and *NEUROD6,* showed a sustained increase in gene expression from day 21 to day 90. Similarly, neuronal cortical layer markers in the deep (*TBR1* and *BCL11B*) and upper layers (*POU3F2* and *SATB2*) showed a similar trend, alongside markers for astrocytes (i.e., *AQP4* and *GFAP*). Still, the elevated expression at day 90 of immature neural markers (*TUBB3* for early born immature neurons, *FABP7* for radial glia (RG), and *EOMES* for intermediate progenitors) suggests the remarkable heterochronicity in the entire process of organoid differentiation.

While neurogenesis heterochronicity in unguided BOs has been observed previously,[12] it remains unknown how it impacts the connectivity and neuronal function. Thus, we performed a detailed analysis of the nature of the intra-organoid long-range projections by labeling organoids with a low dosage of Venus-lentiviral reporter. These results revealed a non-homogeneous distribution of the morphologically distinct neurons and their long-range projections in the whole organoid (Figure 1F). The axo-dendritic network appeared to be more densely distributed in certain regions, forming valley-like paths between adjacent vesicle-like structures within the organoid (Figures 1F and S1J; Video S2). This distinctive distribution of axonal circuitry significantly contributes to the regional variability observed in BO morphology.

Next, we analyzed neuronal activity within the BO through the monitoring of intracellular calcium levels. For this purpose, we infected 90 days old organoids (n = 7) with the AAV7m8 viral vector for the expression of the genetically encoded calcium indicator GCaMP6s under the control of the human *SYN1* promoter. Upon analyzing multiple 10 min-long calcium recordings taken during the next 30 days at different fields of view within each organoid, neuronal activity was evident in all the organoids, even at the immature neuronal network timepoint (Figures 1G and 1H). Infected organoids at later timepoints (180 days) showed mature calcium spikes and neurons generating complex networks, with synchronized collective depolarizations (Video S3). Remarkably, consistent with the considerable cellular variability observed across the different regions within the same organoid, different numbers of active neurons at multiple neurogenic organoid poles were detected, confirming the impact of regional variability in the neuronal function in BOs (Figure S1). The expression of GCaMP in multiple mature neuron subtypes, including GAD65$^+$ GABAergic neurons, within the organoids was confirmed by immunostaining after recordings (Figure S1I).

Functional phenotype detected in Dravet syndrome brain organoids

As a late-onset developmental disorder, DS organoid modeling has been hampered by the inherent variability in the organoid system. Here, we differentiated BOs for 90 days derived from two DS patient-iPSCs carrying the non-synonymous mutation p.A371V:GCT>GTT (DS14 henceforth) and the frameshift mutation p.Val1352CystfrX5 (DS16 henceforth), and a healthy unrelated control iPSC line. In addition, we used H9 (hESC) derived brain organoids as the gold standard differentiation for benchmarking. This maturation stage allowed us to study the DS molecular and functional phenotypes governing the DS epileptogenic state. First, we determined that *SCN1A* gene expression in control-derived organoids significantly increased at mature stages (day 90 vs. day 21 and day 35) (Figure S2E). Next, we examined the expression of SCN1A within the population of mature MAP2$^+$ neurons in both control and DS BOs at day 90 (Figure 2A), as unguided BO differentiation generates both excitatory and inhibitory cortical neurons alongside astroglial cells (Figure 2B). Immunofluorescence analysis revealed no significant differences in the expression of SCN1A among the different genotypes.

To define the onset of the DS phenotype in unguided BOs, all conditions were analyzed at 35 days, when RGs are expanding and neurogenesis starts, and at 90 days of differentiation, when neurogenesis in all cortical layers is established, axonal growth and mature neurons and astrocytes are robustly widespread throughout organoids. No differences in the pace of differentiation were detected up to day 35 among the DS and control genotypes. No differences in the proportion of neural progenitor rosettes (Nestin$^+$, SOX2$^+$, and PAX6$^+$) or early born neurons (β3 Tubulin (Tuj1$^+$) were detected by immunofluorescence on day 35 brain organoids (Figures S3A–S3E).

Similarly, at later stages, the immunophenotypic analysis of the neuronal marker NeuN in DS and control organoids at 90 days of differentiation revealed comparable expression in both groups (Figure 2C). No noteworthy distinctions were observed in the dendrite marker MAP2, the inhibitory neurotransmitter marker GABA, and the astrocyte marker GFAP across all cell lines (Figure 2B). Yet, these markers showed patched expression throughout the organoid under all conditions. This intra-organoid variability was confirmed in H/E and NeuN staining in paraffined organoid serial sections (Figures S4A and S4B), highlighting the intrinsic structural variability in each organoid and confirming the significant intra- and inter-organoid variability independently of the DS and control iPSCs origin.

Next, we evaluated the functional behavior of DS vs. control neurons by monitoring intracellular calcium levels in 100–120 days old organoids (DS n = 8 and control n = 7) expressing GCaMP6s under the control of the human *SYN1* promoter. Acquired spontaneous activity data were visualized in the form of raster plots and analyzed to quantify network activity and functional connectivity, considering groups of the same number of neurons in control and DS (Figures 3A and 3B). First, analysis of the intracellular calcium recordings showed that DS organoids presented a higher number of firing neurons as compared to control ones (Figure 3C). Subsequently, we compared the

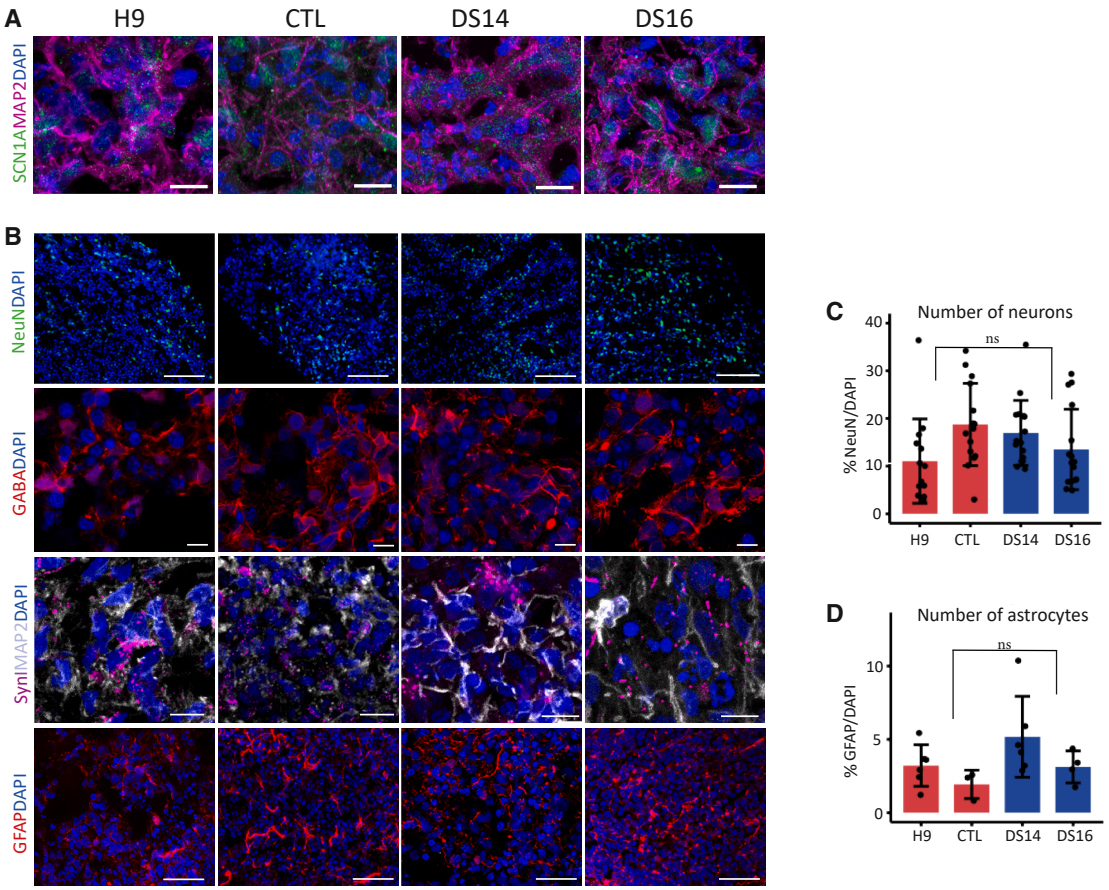


Figure 2. DS brain organoids show imbalanced excitatory-inhibitory circuitry

(A) Immunophenotypic characterization of H9, CTL, DS14, and DS16 brain organoids at day 90 of differentiation, showing SCN1A expression. Scale bar: 15 μm.

(B) Immunophenotypic characterization of H9, CTL, DS14, and DS16 brain organoids at day 90 of differentiation for NeuN, GABA, Syn1, and GFAP markers. Scale bars: 100 μm, 10 μm, 10 μm, and 50 μm, respectively.

(C) Percentage of mature neurons ($NeuN^+$) in 90-day-old brain organoids from H9, CTL, DS14, and DS16 cell lines. Data are represented as mean ± SEM. Wilcoxon rank-sum test showed no statistically significant differences among cell lines (*p* value >0.05).

(D) Percentage of astrocytes ($GFAP^+$) in 90-day-old brain organoids from H9, CTL, DS14, and DS16 cell lines. Data are represented as mean ± SEM, Wilcoxon rank-sum test showed no statistically significant differences among cell lines (*p* value >0.05).

network functional organization in organoids belonging to each genotype class as an approximation to a potential epileptogenic *in vitro* phenotype. The comparison of functional connectivity showed reduced connectivity in DS organoids as compared to control ones (Figure 3D). Further analysis highlighting this phenotypic difference uses global efficiency, a descriptor that captures the capacity for network-wide communication. Global efficiency showed a better performance in control organoids as compared to DS ones (Figure 3E). This could be related to more segregated networks formed by the neurons in DS organoids, which was confirmed by higher community statistics found in this type of organoids, as compared to control ones (Figure 3F). Analysis of clustering and small-world parameters in both types of organoids showed no statistically significant differences (Figures 3G and 3H).

To deeper explore the mechanism responsible for these differences, we generated 2D cultures from DS and control organoids enriched in inhibitory neurons and infected them to express GCaMP6s (approximately 40% of $GAD65^+$/GCaMP6s+ cells) similarly to the above-described BOs (Figures 3I–3L). At differentiation day 50, intracellular calcium recordings were performed on mature neurons from both conditions (DS $n = 3$ and control $n = 3$, Figure 3K). Analysis of the results evidenced a reduction in the number of active neurons in DS cultures as compared to control ones (Figure 3L).

In summary, DS brain organoids show a circuitry-impaired phenotype, even at early maturation stages, characterized by reduced whole-network communications, reproducing channelopathy-related epilepsies.

Transcriptomic analysis indicates an excitatory-inhibitory circuit imbalance in Dravet syndrome brain organoids

DS, like many other DEEs, shows the first clinical symptoms postnatally, during the first two years of life, when the human cerebral cortex is building its circuitry.[27] Therefore, to explore

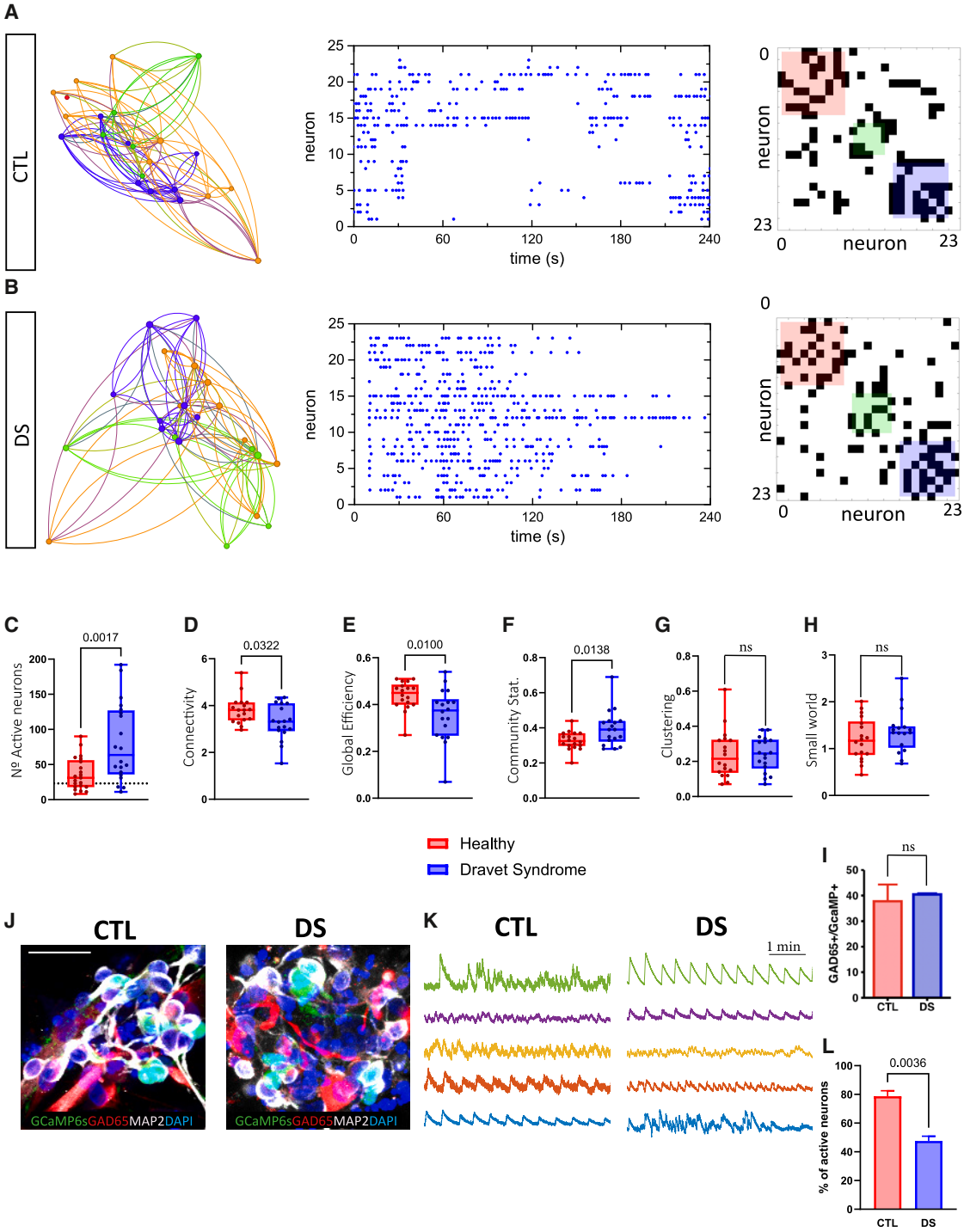


Figure 3. DS brain organoids present defects at the functional level at early stages

(A and B) Calcium imaging analysis of CTL (H9 and CTL iPSC) and DS (DS14 and DS16) derived brain organoids shows connectivity maps (left), raster plots (middle), and connectivity matrices (right).

(C–H) Descriptors of neuronal activity and connectivity in control and DS organoids, (C) number of active neurons, (D) connectivity, (E) community statistic, (F) global efficiency, (G) clustering, and (H) small world. Data are represented as mean ± SEM, and T test was used to test the significance of the results. *p*-values are depicted on every graph.

(I and J) Phenotypic characterization of 2D derived neuronal cultures from CTL and DS genotypes after functional characterization. (I) Percentage of inhibitory neurons, quantified from the ratio of $GAD65^{+}$ neurons to $GCaMP6s^{+}$ stained cells. Co-staining of GCAMP6s with GAD65 and MAP2 shows the presence of

(legend continued on next page)

whether the underlying phenotypic changes appear during neurogenesis or during axonal network outgrowth and synaptogenesis, we performed RNAseq at day 35 and day 90 organoid maturation stages. At the selected time points, neurogenesis is soundly established throughout the organoid, and neuronal connectivity is being established, respectively. The late onset molecular phenotype is evidenced at the transcriptomic level by PCA comparing day 35 and day 90 in control and DS (Figure 4A). The longitudinal transcriptomic analysis suggests that the DS phenotype is established at day 90, while no transcriptional phenotype is detected at day 35. At this stage, only 15 differentially expressed (DE) genes in DS vs. control could be detected (Figure S3F; Table S1).

Compatible with late-onset channelopathy in patients with DS, the bulk transcriptomic analysis at day 90 showed that 768 out of 1205 genes were upregulated and 437/1205 were downregulated between the control and DS organoids (Table S2). Gene Set Enrichment Analysis (GSEA) results, ranked according to their significance (p-adjusted value), indicated that the most significantly dysregulated biological processes were associated with essential glutamatergic and GABAergic synapse formation and downregulation of cilia organization (Figures 4B and 4C; Table S3), two processes highly associated with synaptic formation, connectivity, and homeostasis.

Among genes differentially upregulated in DS organoids, a remarkable correlation was found with genes driving other epileptic syndromes, such as *SYN1*, *SCN2A*, *KCNC2,* and multiple *GRIN* genes (*GRIN2B* and *GRIN3B*), all involved in neuronal excitability, connectivity, and brain plasticity mechanisms. Instead, *SCN1A*, the DS pathogenesis driving gene, did not show differential expression (Figure 4D). Moreover, DS present an upregulation of several GABA receptors (Figure 4C), commonly expressed in excitatory neurons,[28] while transcriptomic levels of glutamate receptors (i.e., NMDA and AMPA receptors) or genes involved in GABA synthesis and transport (i.e., *GAD1*, *GAD2*, *ALDH5A1*, *ABAT*) are not dysregulated in DS organoids, suggesting a putative compensatory mechanism to the limited inhibitory synaptic activity hypothesized in DS.

No significant changes in cortical excitatory neuronal markers, such as *TBR1*, *FOXP2*, *BCL11B*, *EMX2,* and *EMX1*, were detected, nor was a significant downregulation of astrocytic markers, such as *GFAP* and *VIM*, observed (Figure 4D), supporting the immunophenotypic data. The lack of gene expression differences for regional and layer transcriptional biomarkers in the bulk transcriptome suggests that the differentiation pace is similar between control and DS brain organoids, as suggested by immunofluorescence. Therefore, the transcriptomic results rely mostly on the imbalance in the excitatory and inhibitory synaptic signaling and connectivity. Notably, in response to this imbalance, DS organoids activate intrinsic pathways to compensate for the increased number of active neurons, potentially leading to alterations in synaptic plasticity and overall network dynamics.

Convolutional neural networks' prediction of brain organoids' phenotype classification

In DS-derived BOs, the pathogenic phenotype is associated with abnormal axonal circuitry. However, accurately defining this phenotype amidst intrinsic variability remains challenging when using conventional immunofluorescence markers. To overcome these limitations and enable real-time evaluation of circuitry changes within a genotype-specific background, we employed Cellbrite staining in combination with live imaging.

Thus, we aimed to determine whether the DS-associated phenotype, involving the neuronal axonal network, could be systematically identified while minimizing intra-organoid variability and late onset phenotype.

To this purpose, we leveraged the neuronal circuit tracer resolution of Cellbrite staining to label the neuronal network *in vitro* and established an integrated pipeline for circuit tracing, live imaging of the whole organoid, and DL analysis (Figure 5A). Whole Cellbrite stained organoids were imaged in depth (~500 μm imaging 1 plane every 50 μm; Figure S4C) using wide-field microscopy with digital sectioning at low magnification (10X). This systematic acquisition, alongside the digital z stack, allowed the subsequent analysis of the organoid surface through the analyzed 500 μm volume acquired in a top-to-bottom manner. This step was followed by extensive pre-processing (Figure S4D), encompassing the following serial steps: 1) whole surface stitching considering all z-stacks, 2) intensity and pixel (px) sharpness correction, 3) partition of stitched corrected image into 224x224 px, and 4) removal of non-QC images based on px focus sharpness, artifacts due to the reconstruction process and background, resulting in corrected organoid region images (CORIs). Henceforth, the integrated pipeline and analysis will be named Image Phenotype Network (ImPheNet). A total of 1619 images of H9 and DS14 (from 27 to 28 organoids respectively) were used for training, whereas for testing, images obtained from 45 control (H9 and control iPSC) and 38 DS organoids (DS14 and DS16) were used. All organoids were imaged in 6 independently obtained batches. Each CORI was independently classified by ImPheNet, generating a prediction score ranging from 0 (Dravet Syndrome) to 1 (Control) (Figures 5A–5D). The model achieved an accuracy of 0.732 when analyzing CORIs individually (Figure S4E). Given the substantial intra-organoid variability, we further consolidated the CORI prediction values into an adjusted classification score for each whole organoid, estimated from the training dataset (see STAR Methods Section for details). These scores are named as CONTROL SCORE and DRAVET SCORE, resulting in 0 = totally Dravet and 1 = totally Control (Figures 5B–5D). Using this classification score, the identified phenotype matched with the corresponding genotype with an accuracy of 0.967 (Figure S4F).

GCAMP6s in interneurons and in the general population of neurons. Data are represented as mean ± SEM, and the Wilcoxon rank-sum test shows no statistically significant differences (p value >0.05). Scale bar: 25 μm.

(K) Calcium imaging activity traces of individual $Syn1^+$ neurons from 2D derived neuronal cultures infected with a GCaMP6s AAV.

(L) Percentage of active neurons in CTL and SD analyzed with 2D cultures. Data are represented as mean ± SEM. The Wilcoxon rank-sum test revealed statistically significant differences ($p < 0.05$).

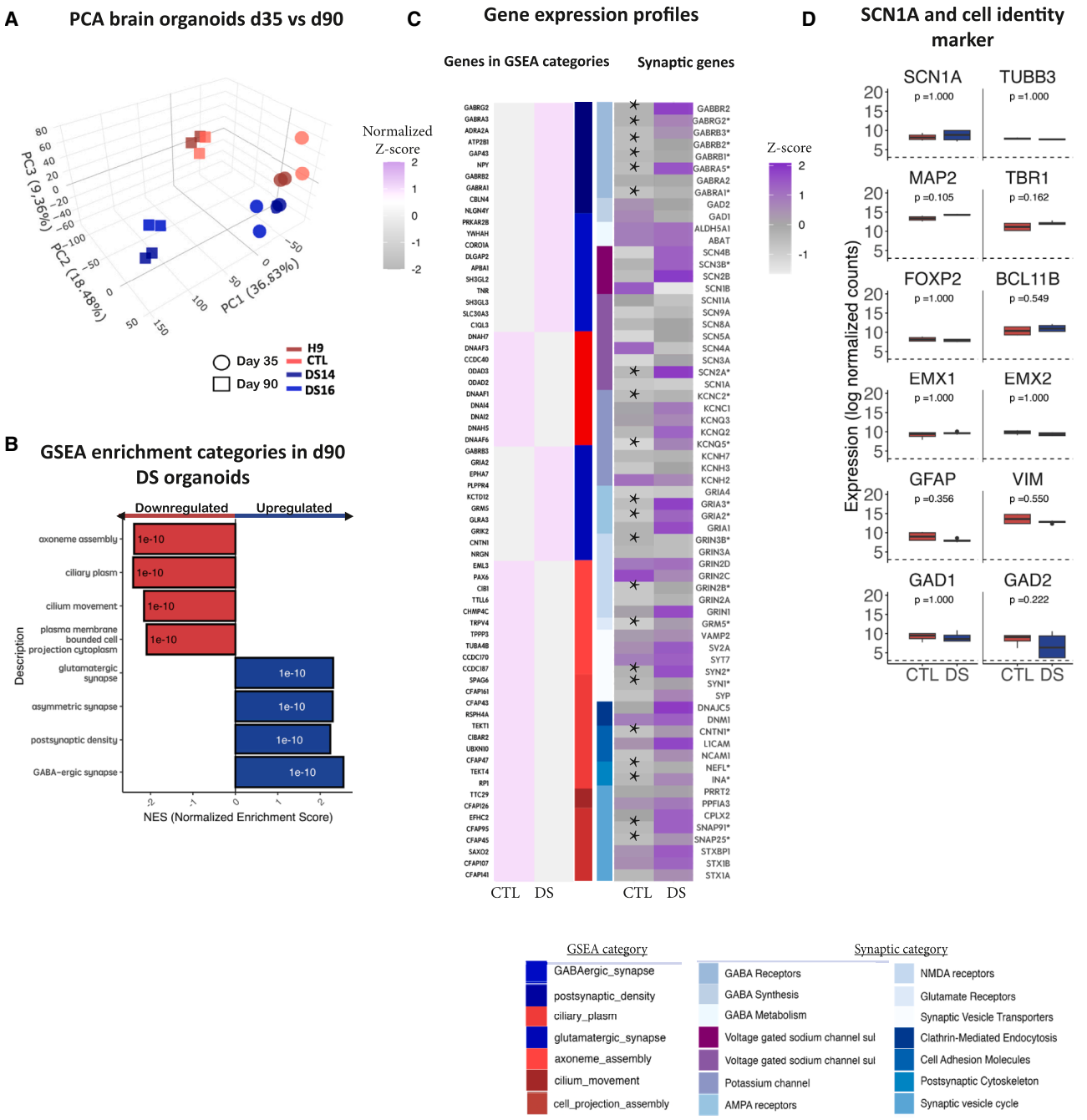


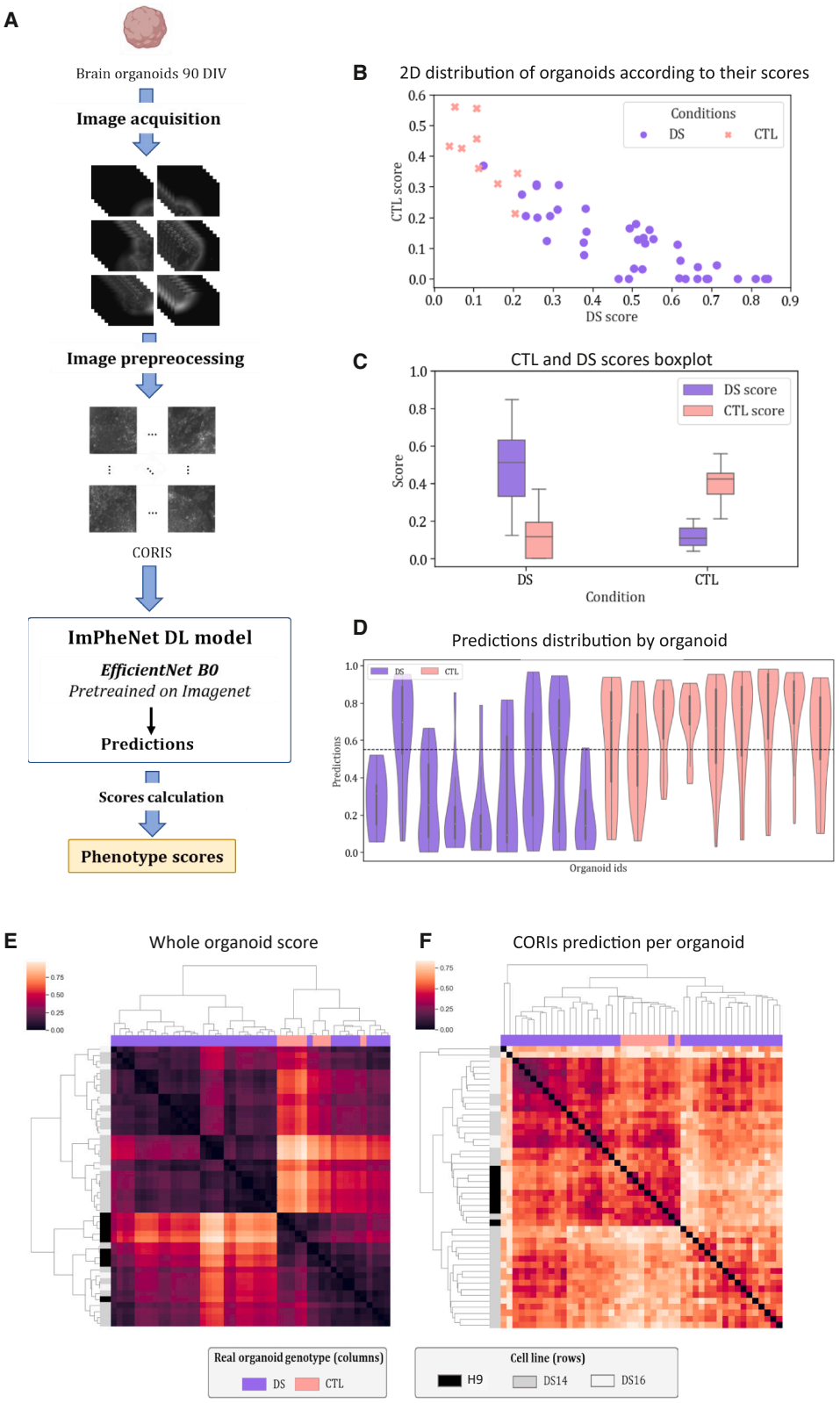
Figure 4. DS organoids acquire a distinct phenotype at later stages of differentiation

(A) Principal component analysis (PCA) plot illustrates that d35 organoids exhibit similar transcriptomic profiles, while day-90 organoids show pronounced phenotypic differences.

(B) GSEA-enriched categories in DS versus CTL brain organoids. Categories in blue are upregulated in DS organoids, and those in red are upregulated in CTL organoids, selected based on *p*-values and biological relevance.

(C) Expression profile of genes included in the highlighted GSEA categories, with their respective expression in normalized Z-scores (left). Heatmap displays relative expression (0 = downregulated in gray, 1 = upregulated, in purple) of DE genes at day 90 from the GSEA-enriched categories shown in B. In the right panel, expression profile of synaptic genes in DS and CTL day-90 brain organoids, with Z-scores calculated from the mean count distribution. Differentially expressed (DE) genes are highlighted with an asterisk (*).

(D) Expression profile of the *SCN1A* gene and other cell identity markers in day-90 brain organoids. No significant differences between groups were detected in terms of gene expression (*p*-value from DESeq2 analysis).



(legend on next page)

The intra-organoid variability is a confounding factor when it comes to predicting the organoids' phenotype. This variability is reflected in the dispersion observed in the CORIs prediction values for the same organoid (Figures 5D, S4G, and S4H). When comparing the data distribution of CORI's classification and whole organoid adjusted scores, the dissimilarity among each organoid belonging to the same class is reduced (Figure 5E). Notably, the variability due to batch effect is buffered using the ImPheNet algorithm independently of whether the classification is carried out on whole scores or on single image classification (CORIs) (Figures 5E and 5F). In conclusion, our results demonstrate that the ImPheNet system enables robust and accurate classification of DS-associated phenotypes through live imaging analysis, providing a powerful tool for studying axonal network abnormalities in patient-derived organoids.

Image phenotype network classification of anti-seizure drugs toxicity in Dravet syndrome brain organoids

In DS, as in many other rare disorders, limited randomized controlled trials have hindered evidence-based treatments, and the only ones available include stiripentol (STP), cannabidiol (CBD), and fenfluramine (FFA). Treatment guidelines recommend valproic acid (VPA) as the preferred first-line treatment.[29] VPA can reduce seizure frequency and severity, though achieving seizure freedom is rare. Sodium channel blockers, such as phenytoin (PHT) and lamotrigine (LAM), are not recommended due to negative effects on seizure frequency and cognitive outcomes.[30] Second-line options outlined in the guidelines include STP with VPA and clobazam, topiramate, and the ketogenic diet. Due to the potential negative effects of antiseizure drugs in patients with DS, we aimed to explore the impact of other known antiepileptic treatments in ImPheNet as a tool for drug testing in DS BOs. All treatment conditions were applied acutely for one week to mature brain organoids (day 90). Cellbrite stained organoids were imaged pre- and post-treatment, and no evident differences in the morphology nor in fluorescence intensity among them were detected upon treatment (Figure 6A). Subsequently, the ImPhenet pipeline was used as previously described. Two cohorts of brain organoids were generated for the training dataset: DS untreated brain organoids and those treated with the sodium channel blockers lamotrigine and phenytoin (Na INH class), serving as markers of toxicity-related outcomes. Once the model was trained and validated, we further tested the potential toxicity of VPA, CBD, and FFA in DS brain organoids.

During model development, it was detected that adjusted classification scores resolved the classification of toxic treatment events better than CORI's predictions (CORI's-Accuracy 0.759 vs. whole organoid score accuracy 0.941; Figures 6B, 6C, S5E, and S5F). Notably, recently approved drugs for DS, CBD, and FFA exhibited reduced levels of the Na INH class component, followed by VPA (Figure 6C), suggesting that they show lower levels of toxicity. Transcriptomic analysis of VPA treated DS and control organoids reveals that the antiseizure drug induced significant changes in both genotypes (Figures S5F and S5G), promoting the reversion of the transcriptomic profile of genes that were dysregulated in the context of DS. These results were validated in parallel using organoid histological analysis, encompassing neuronal and glial markers, alongside activated caspase 3 (aCasp3) immunostaining to determine a putative increase in apoptosis (Figures 6A and 6D). No significant changes could be detected either in the cell type presence or apoptosis in the treatments, suggesting that Na INH class drugs can affect functionally in the neuronal network rather than in the cytoarchitecture in the brain organoids. Altogether, the ImPheNet arises as a relevant tool to detect toxicity events in DS-derived brain organoids that cannot be detected by conventional immunostaining methods.

DISCUSSION

Brain organoids offer significant advantages for studying brain development, disease, and function, particularly their ability to intrinsically form neuronal networks, making them valuable for modeling disorders that impact neural connections. However, they face two key issues: their largely heterochronic maturation and inherent cellular and regional variability. In this study, we propose a systematic DL-driven analysis, the ImPheNet, to overcome these limitations. The DL-based approach that we have developed here, the ImPheNet, allowed us to perform live imaging classification of DS-derived organoids. The DEE we employed as a paradigm of the late-onset pharmaco-resistant neurodevelopmental disorder. Moreover, we benchmarked the DL detected phenotype with molecular and functional analysis, which revealed an imbalanced inhibitory-excitatory neural circuitry in DS.

Intra- and inter-organoid variability

The use of BOs in disease modeling and translational studies has been hampered by the substantial variability inherent to the organoid model. BO differentiation protocols start with a defined number of self-aggregating PSCs, that after neural induction, generate multiple neurogenic centers or rosettes.[31] In unguided organoid differentiation protocols, the wide range of brain cellular diversity is generated following the clonality of the NPC clusters distributed throughout the organoid neuroepithelium at

Figure 5. ImPheNet predictive model

(A) Workflow of the ImPheNet AI-based model: from image preprocessing to genotype-related phenotype prediction.

(B) Representation of "CTL score" (y axis) and "DS score" (x axis) per organoid, labeled based on their real genotype (H9 vs. DS14).

(C) Boxplot of CTL and DS score ratios per genotype.

(D) Violin plot of phenotypic predictions (CORIs) per organoid.

(E and F) Clustermap using the Jensen-Shannon distance (left) between integrated whole-organoid histograms of predictions and (right) clustermap using the Euclidean distance between the computed scores, for each CORI grouped per organoid. These heatmaps show how the predictive power dramatically increases when the whole organoid is considered, compared to considering only regional information, highlighting the need for an integrated organoid analysis to reduce the intra-organoid variability bias.

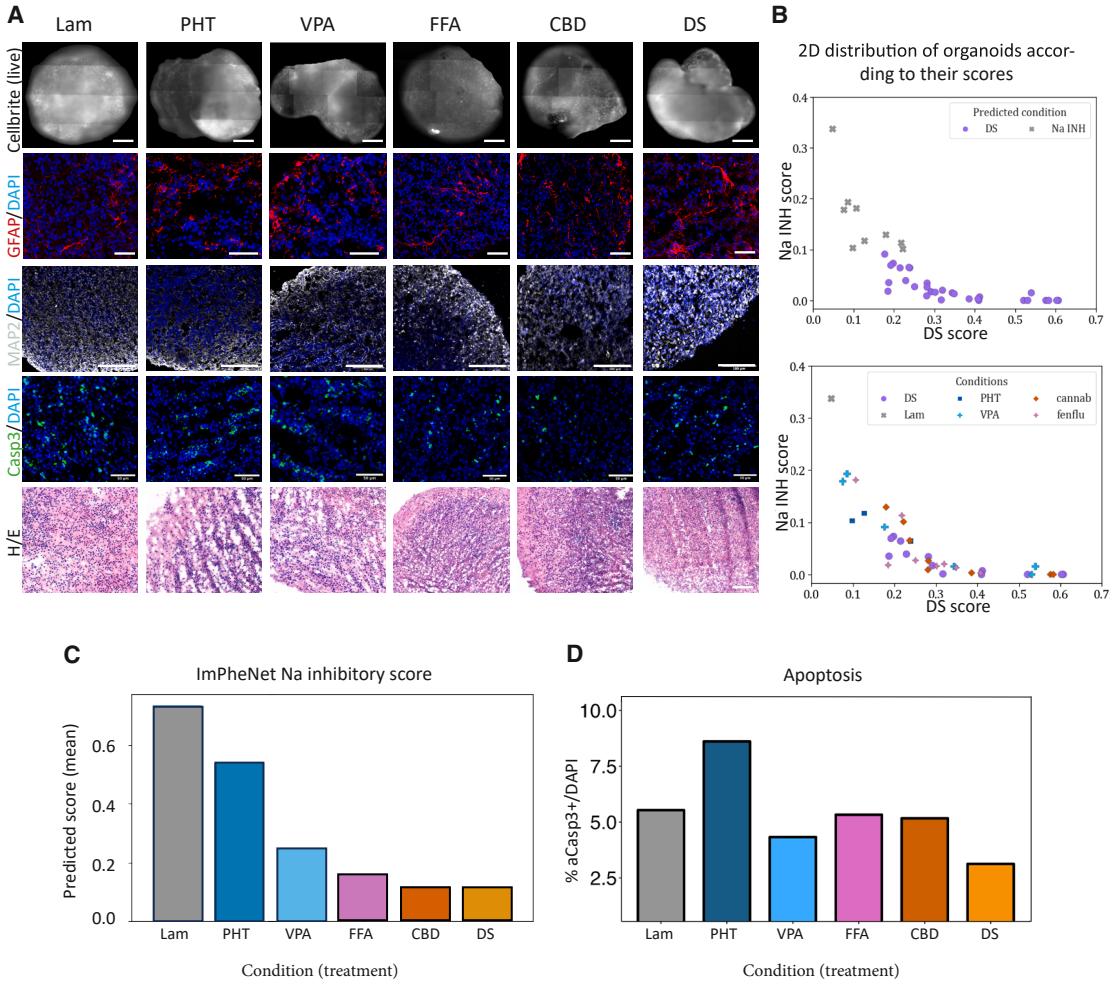


Figure 6. ImPheNet prediction in anti-seizure treatments

(A) Morphological and immunophenotypic analysis of antiseizure drug effect on DS day 90 brain organoids. Cellbrite-stained organoids imaged after 7 days of treatment (Row 1). Immunophenotypic (astrocytes-GFAP; neuronal dendrites-MAP2; apoptosis-activated CASPASE3) characterization (Rows 2–4) and Hematoxylin and eosin (H/E) staining (Row 5) of brain organoids exposed to Lamotrigine (Lam), Phenytoin (PHT), Valproat (VPA), Fenfluramine (FFA), Cannabidiol (CBD). These results indicated limited morphological and cellular changes. Scale bars: 400 μm, 50 μm, 100 μm, 50 μm, and 50 μm, from top to bottom, respectively.

(B) 2D distribution of DS and Na INH scores per organoid, colored by predicted class (up) and treatment (down).

(C) Barplot shows the Na INH score of the different treatments in DS brain organoids calculated with ImPheNet. Na INH score is represented by the ratio of the NA INH CORIs.

(D) Percentage of activated Caspase-3 cells in drug-induced apoptosis analysis by IF staining. Data are represented as a median. Wilcoxon rank-sum test revealed no significant differences among treatments (2 independent experiments/n = 3 organoids per condition (p value >0.05).

very early stages.[12] Thus, this regional patterning segregation occurs as early as day 15 of differentiation, making organoids' regional variability very liable to small signaling variations in the culture media, as well as other deviations in the protocol (stemness status, survival to seeding, small molecule bioavailability, and morphological arrangement).[31] The ability of BOs to grow for several months in suspension enables long-term reconstruction of a complex neuronal network that rearranges over time.[15] Moreover, the suspension nature of the 3D model growth impairs the systematic positioning of the organoids for longitudinal analysis, increasing the morphological variability perception. In this study, we tackled the contribution of the neuronal network and its functional capacity to the given inter- and intra-organoid underlying variability. Staining axonal networks with Cellbrite (cytoplasmic membrane dye) and Venus reporter lentiviral low dosage infection, we determined that BOs axons extend bundles to functionally connect far-distance regions, projecting from multiple neurogenic centers, similarly to other protocols using air-liquid interface.[15] The non-homogenous distribution of the neuronal connections and their constant remodeling as the organoid matures constitute a great source of the observed organoid variability. Using calcium imaging, we did not observe genotype-related differences in the transmission of the information across different regions considered separately, although we can

distinguish reduced global efficiency in DS as compared to control organoids when considering all regions grouped per organoid. This strong reduction in inter-organoid variability makes organoids from the same genotype comparable between them from a functional point of view and distinguishable from the others in the same way the ImPheNet does, and thus, highlights brain organoids as an excellent tool for brain network analysis and disease modeling.

Integrative method for brain organoid phenotyping

AI methods, including convolutional neural networks (CNNs), are especially suited to analyze complex image data derived from brain organoids.[32–34] Live imaging of medium-large 3D densely populated structures encompasses a good number of optical challenges, including size, systematic position, light refraction, and penetration. Here, we propose a reductionist approach using Cellbrite dye to label the neural membrane, followed by live imaging on a wide-field microscope. Using the ImPhenet, we determined that only when brain organoids are contemplated as a whole, instead of as the mean of multiple regions, does the DS phenotype arises. The ImPheNet scoring algorithm significantly reduced the inter-batch variability, providing a robust analysis methodology for further applications, such as *in vitro* drug testing.

Patients with DS are frequently pharmacoresistant, and few randomized controlled trials exist.[29,35] In this study, we provide a proof-of-concept that the ImPheNet algorithm can be leveraged to evaluate *in vitro* the toxic potential of antiseizure drugs. The ImPheNet algorithm classifies the recently approved drugs, CBD and FFA, as the least toxic in DS, followed by VPA, the first line and most commonly used drug in DS treatment and other epileptic encephalopathies. Although more data are needed in this context, with further drugs and more patient-derived iPSCs. This is a promising result to advance in the therapeutic approaches to epileptic encephalothies.

Brain organoid modeling of Dravet syndrome

The primary genetic cause of DS is the presence of pathogenic variants in the *SCN1A* gene, which encodes a subunit of the voltage gated sodium channel Nav1.1.[36] *Scn1a* mutant mouse models have shed light on the cell types implicated in DS.[37–39] However, not a full neuropathology reconstruction has been achieved, mainly due to inherent evolutionary differences in the human brain construction, relating to the multiple types and number of neurons as well as to the higher complexity of the human neuronal connectome and synapse plasticity.[40–44] Our data obtained from DS brain organoids indicate that at a transcriptomic level, the DS organoid phenotype is strongly associated with synaptic dysregulation and function, and not with cellular subtypes. This is in line with recent studies on *SCN1A* knockout brain organoids, which also report elevated levels of synaptic components at the protein level.[45] Notably, these differences were translated into changes at the circuitry level, where we identified significant changes in the construction of the neuronal network, pointing toward and imbalance in the excitatory-inhibitory network. Although at early stages (90–120 days) of differentiation, collective events were not detectable by intracellular calcium recordings, differences between control and DS organoids were notable in the developing networks. Higher numbers of active neurons in DS organoids were not accompanied by increased global efficiency. In contrast, higher segregation observed in DS organoids as compared to control organoids resulted in less efficient networks, which may lead to increased excitation at later timepoints. Our results add to those of multiple labs specialized in the iPSC modeling of neurodevelopmental disorders, supporting the relevance of alterations in neuronal circuitry.[4,6,22,46] Altogether, our data support expanding the use of BOs modeling to complex neurodevelopmental disorders characterized by circuitry unbalance. This cutting-edge approach addresses the limitation of BOs' use by establishing a whole-organoids strategy for the genotype-related phenotype analysis.

To summarize, we have developed a novel approach to analyze phenotypes related to neuronal axonal network changes using a reductionist and automated way, the ImPheNet, which is compatible with longitudinal brain organoid studies, like, for instance, *in vitro* drug testing. Moreover, we provide a comprehensive study of the source of the variability in BOs, and we propose a tool to overcome it. Last, we provide insight into the neuropathogenesis of DS and the molecular effects of VPA as a DS antiseizure drug.

Limitations of the study

These findings should be viewed as a proof-of-concept of the use of AI methods to discrimite among phenotypes in DS brain organoids. Among the main flaws of the study, it is important to highlight that unguided cerebral organoids introduce heterogeneity and regional heterochrony that ImPheNet mitigates analytically rather than biologically. The choice of protocol was made to preserve cellular diversity in BO, which is better represented in unguided than in guided organoids. This also, phenotyping was centered on ~90–120 days and on wide-field, surface live imaging with Cellbrite; deeper structures and later stages remain natural extensions. Bulk RNA-seq at two time points supports a late-emerging phenotype, though single-cell or spatial profiling could refine cell-type-specific interpretations, and the inclusion of longer differentiation might contribute to better characterizing the DS pathogenic phenotype. Only two *SCN1A* variants plus unrelated controls were used in this article, while many other mutations in SCN1A have been identified in DS. Also, the use of unrelated control vs. no-isogenic pairs was a choice since it will be able to better discriminate among the phenotype and genetic confounding factors in an automatized DL model, while isogenic pairs will better contribute to understanding the pathophysiology of the mutations. ImPheNet was trained/validated on in-house data labeled by genotype; multi-site benchmarking and interpretability analyses would further establish robustness and biological linkage. Drug testing was acute and anchored to sodium-channel blocker reference toxicity; dose-response, chronic/washout designs, and pharmacodynamic or functional-rescue readouts are promising next steps. Transferability to guided organoids or additional DEEs remains to be systematically evaluated.

RESOURCE AVAILABILITY

Lead contact

Further information and requests for resources and reagents should be directed to and will be fulfilled by the lead contact, Sandra Acosta (sandra.acosta@ub.edu).

Materials availability

This study did not generate new unique reagents.

Data and code availability

- Data: RNA-seq data have been deposited at GEO and are publicly available as of the date of publication. Accession numbers are listed in the key resources table GSE256142.
- Code: All original code has been deposited at Zenodo, and is publicly available (https://doi.org/10.5281/zenodo.10636044).
- Additional information: Any additional information required to reanalyze the data reported in this article is available from the lead contact upon request.

ACKNOWLEDGMENTS

We thank Dr. Oliver, Dr. Fiore, and Dr. Ortega for their insights into the article. We thank IDIBELL and UB Scientific Platforms, especially Dr. Torrejón at Bellvitge- Microscopy Unit CCTIUB, and María Calvo and Gemma Martín at Clinic-Microscopy Unit CCiTUB, for their constant technical assistance in the experimental execution, and the UPF Genomics Platform for the execution of RNAseq. S.A. is a Serra-Hunter Assistant Professor Fellow of the Generalitat de Catalunya. This project has been funded by Caixa Impulse (CXI20-0002) to S.A. and O.L., and AGAUR Llavor (2021) to S.A. J.S. and S.A. acknowledge support from grants PID2021-128208NB-100 and PID2022-137713NB-C22, respectively, funded by MCIU/AEI/10.13039/501100011033 and by ERDF/EU. D.T. acknowledges support from grant CNS2023-143862, funded by MCIN/AEI/10.13039/501100011033 and Next Generation EU/PRTR. D.T. and J.S. also acknowledge Generalitat de Catalunya under grants 2021SGR01086 and 2021-SGR-00450, respectively. This work has received funding from the European Union's Horizon 2020 research and innovation program under the grant agreement NeuChiP No. 964877 (A.-C.H, J.S., and D.T.). E.E. is funded by a Ramon y Cajal Fellowship (MICINN).

AUTHOR CONTRIBUTIONS

S.A., D.T., O.L., and I.T. conceptualized and designed the study; S.A., D.T., and O.L. oversaw the implementation and management of all experiments; I.T. generated and analyzed; B.O. used in the study, performed immunostaining and RNAseq studies, drug testing, and live imaging experiments; A.M. generated and implemented the deep learning analytical pipeline for organoid phenotyping and drug response screening; I.P. and E.E. contributed to the generation of the LV virus for transduction and related cell culture performance; L.G.G. performed imaging on LV-infected organoids; A.M.S., A.O.G., A.C.H., D.T., and J.S. conducted calcium imaging experiments and performed neuronal network analysis; R.P. and N.R. contributed to the histological analysis of BO. S.A., I.T., A.N., and D.T. wrote the original article draft, which was reviewed by all co-authors and further edited; All authors read and approved the final article.

DECLARATION OF INTERESTS

SA and OL are shareholders of the OrganAID Holdings.S.L.

STAR★METHODS

Detailed methods are provided in the online version of this paper and include the following:

- KEY RESOURCES TABLE
- EXPERIMENTAL MODEL AND STUDY PARTICIPANT DETAILS
  - Brain organoids generation
  - 2D neuronal cultures preparation
- METHOD DETAILS
  - Immunofluorescence analysis
  - RNA preparation
  - RNAseq analysis
  - Histological staining
  - Intracellular calcium recording analysis
  - Low dosage viral infection
  - Live imaging
  - Drug testing experiment
  - Image preprocessing
  - ImPheNet: Dataset generation
  - ImPheNet: DL model
  - ImPheNet: DL model results
- QUANTIFICATION AND STATISTICAL ANALYSIS

SUPPLEMENTAL INFORMATION

Supplemental information can be found online at https://doi.org/10.1016/j.isci.2025.113831.

Received: April 30, 2024
Revised: December 27, 2024
Accepted: October 17, 2025
Published: October 23, 2025

REFERENCES

1. Lancaster, M.A., Renner, M., Martin, C.A., Wenzel, D., Bicknell, L.S., Hurles, M.E., Homfray, T., Penninger, J.M., Jackson, A.P., and Knoblich, J.A. (2013). Cerebral organoids model human brain development and microcephaly. Nature *501*, 373–379.
2. Albanese, A., Swaney, J.M., Yun, D.H., Evans, N.B., Antonucci, J.M., Velasco, S., Sohn, C.H., Arlotta, P., Gehrke, L., and Chung, K. (2020). Multiscale 3D phenotyping of human cerebral organoids. Sci. Rep. *10*, 21487.
3. Velasco, S., Kedaigle, A.J., Simmons, S.K., Nash, A., Rocha, M., Quadrato, G., Paulsen, B., Nguyen, L., Adiconis, X., Regev, A., et al. (2019). Individual brain organoids reproducibly form cell diversity of the human cerebral cortex. Nature *570*, 523–527.
4. Birey, F., Andersen, J., Makinson, C.D., Islam, S., Wei, W., Huber, N., Fan, H.C., Metzler, K.R.C., Panagiotakos, G., Thom, N., et al. (2017). Assembly of functionally integrated human forebrain spheroids. Nature *545*, 54–59.
5. Kadoshima, T., Sakaguchi, H., Nakano, T., Soen, M., Ando, S., Eiraku, M., and Sasai, Y. (2013). Self-organization of axial polarity, inside-out layer pattern, and species-specific progenitor dynamics in human ES cell–derived neocortex. Proc. Natl. Acad. Sci. USA *110*, 20284–20289.
6. Trujillo, C.A., Gao, R., Negraes, P.D., Gu, J., Buchanan, J., Preissl, S., Wang, A., Wu, W., Haddad, G.G., Chaim, I.A., et al. (2019). Complex Oscillatory Waves Emerging from Cortical Organoids Model Early Human Brain Network Development. Cell Stem Cell *25*, 558–569.e7.
7. Saglam-Metiner, P., Devamoglu, U., Filiz, Y., Akbari, S., Beceren, G., Goker, B., Yaldiz, B., Yanasik, S., Biray Avci, C., Erdal, E., and Yesil-Celiktas, O. (2023). Spatio-temporal dynamics enhance cellular diversity, neuronal function and further maturation of human cerebral organoids. Commun. Biol. *6*, 173.
8. Lancaster, M.A., and Knoblich, J.A. (2014). Organogenesis in a dish: Modeling development and disease using organoid technologies. Science *345*, 1247125.
9. Lancaster, M.A., and Knoblich, J.A. (2014). Generation of cerebral organoids from human pluripotent stem cells. Nat. Protoc. *9*, 2329–2340.
10. Mora-Jimenez, L., Valencia, M., Sanchez-Carpintero, R., Tønnesen, J., Fadila, S., Rubinstein, M., Gonzalez-Aparicio, M., Bunuales, M., Fernandez-Pierola, E., Nicolas, M.J., et al. (2021). Transfer of SCN1A to the brain of adolescent mouse model of Dravet syndrome improves epileptic, motor, and behavioral manifestations. Mol. Ther. Nucleic Acids *25*, 585–602.
11. Quadrato, G., Nguyen, T., Macosko, E.Z., Sherwood, J.L., Min Yang, S., Berger, D.R., Maria, N., Scholvin, J., Goldman, M., Kinney, J.P., et al. (2017). Cell diversity and network dynamics in photosensitive human brain organoids. Nature *545*, 48–53.

12. He, Z., Maynard, A., Jain, A., Gerber, T., Petri, R., Lin, H.C., Santel, M., Ly, K., Dupré, J.S., Sidow, L., et al. (2022). Lineage recording in human cerebral organoids. Nat. Methods *19*, 90–99.

13. Knight, G.T., Lundin, B.F., Iyer, N., Ashton, L.M., Sethares, W.A., Willett, R.M., and Ashton, R.S. (2018). Engineering induction of singular neural rosette emergence within hPSC-derived tissues. eLife *7*, e37549.

14. Qian, X., Nguyen, H.N., Song, M.M., Hadiono, C., Ogden, S.C., Hammack, C., Yao, B., Hamersky, G.R., Jacob, F., Zhong, C., et al. (2016). Brain-Region-Specific Organoids Using Mini-bioreactors for Modeling ZIKV Exposure. Cell *165*, 1238–1254.

15. Giandomenico, S.L., Sutcliffe, M., and Lancaster, M.A. (2021). Generation and long-term culture of advanced cerebral organoids for studying later stages of neural development. Nat. Protoc. *16*, 579–602.

16. Di Lullo, E., and Kriegstein, A.R. (2017). The use of brain organoids to investigate neural development and disease. Nat. Rev. Neurosci. *18*, 573–584.

17. Scheffer, I.E., Berkovic, S., Capovilla, G., Connolly, M.B., French, J., Guilhoto, L., Hirsch, E., Jain, S., Mathern, G.W., Moshé, S.L., et al. (2017). ILAE classification of the epilepsies: Position paper of the ILAE Commission for Classification and Terminology. Epilepsia *58*, 512–521.

18. Ogiwara, I., Iwasato, T., Miyamoto, H., Iwata, R., Yamagata, T., Mazaki, E., Yanagawa, Y., Tamamaki, N., Hensch, T.K., Itohara, S., and Yamakawa, K. (2013). Nav1.1 haploinsufficiency in excitatory neurons ameliorates seizure-associated sudden death in a mouse model of Dravet syndrome. Hum. Mol. Genet. *22*, 4784–4804.

19. Catterall, W.A., Kalume, F., and Oakley, J.C. (2010). NaV1.1 channels and epilepsy. J. Physiol. *588*, 1849–1859.

20. Yu, F.H., Mantegazza, M., Westenbroek, R.E., Robbins, C.A., Kalume, F., Burton, K.A., Spain, W.J., McKnight, G.S., Scheuer, T., and Catterall, W.A. (2006). Reduced sodium current in GABAergic interneurons in a mouse model of severe myoclonic epilepsy in infancy. Nat. Neurosci. *9*, 1142–1149.

21. Alex, C.B., Richard, P.M., and Rod, C.S. (2012). SCN1A mutations in Dravet syndrome: Impact of interneuron dysfunction on neural networks and cognitive outcome. Epilepsy Behav. *23*, 177–186.

22. Samarasinghe, R.A., Miranda, O.A., Buth, J.E., Mitchell, S., Ferando, I., Watanabe, M., Allison, T.F., Kurdian, A., Fotion, N.N., Gandal, M.J., et al. (2021). Identification of neural oscillations and epileptiform changes in human brain organoids. Nat. Neurosci. *24*, 1488–1500.

23. Liu, H., Zhao, Y., Yang, F., Lou, X., Wu, F., Li, H., Xing, X., Peng, T., Menze, B., Huang, J., et al. (2022). Preoperative Prediction of Lymph Node Metastasis in Colorectal Cancer with Deep Learning. BME Front. *2022*, 9860179.

24. Esteva, A., Kuprel, B., Novoa, R.A., Ko, J., Swetter, S.M., Blau, H.M., and Thrun, S. (2017). Dermatologist-level classification of skin cancer with deep neural networks. Nature *542*, 115–118.

25. Li, T., Tong, W., Roberts, R., Liu, Z., and Thakkar, S. (2020). Deep Learning on High-Throughput Transcriptomics to Predict Drug-Induced Liver Injury. Front. Bioeng. Biotechnol. *8*, 562677.

26. Raschka, S., and Kaufman, B. (2020). Machine learning and AI-based approaches for bioactive ligand discovery and GPCR-ligand recognition. Methods *180*, 89–110.

27. Huttenlocher, P.R. (1979). Synaptic density in human frontal cortex — Developmental changes and effects of aging. Brain Res. *163*, 195–205.

28. Datta, D., Arion, D., and Lewis, D.A. (2015). Developmental Expression Patterns of GABAA Receptor Subunits in Layer 3 and 5 Pyramidal Cells of Monkey Prefrontal Cortex. Cereb. Cortex *25*, 2295–2305.

29. Cardenal-Muñoz, E., Auvin, S., Villanueva, V., Cross, J.H., Zuberi, S.M., Lagae, L., and Aibar, J.Á. (2021). Guidance on Dravet syndrome from infant to adult care: Road map for treatment planning in Europe. Epilepsia Open *7*, 11–26.

30. Wirrell, E.C. (2016). Treatment of Dravet Syndrome. Can. J. Neurol. Sci. *43*, S13–S18.

31. Martins-Costa, C., Pham, V.A., Sidhaye, J., Novatchkova, M., Wiegers, A., Peer, A., Möseneder, P., Corsini, N.S., and Knoblich, J.A. (2023). Morphogenesis and development of human telencephalic organoids in the absence and presence of exogenous extracellular matrix. EMBO J. *42*, e113213.

32. Kassis, T., Hernandez-Gordillo, V., Langer, R., and Griffith, L.G. (2019). OrgaQuant: Human Intestinal Organoid Localization and Quantification Using Deep Convolutional Neural Networks. Sci. Rep. *9*, 12479.

33. Metzger, J.J., Pereda, C., Adhikari, A., Haremaki, T., Galgoczi, S., Siggia, E.D., Brivanlou, A.H., and Etoc, F. (2022). Deep-learning analysis of micropattern-based organoids enables high-throughput drug screening of Huntington's disease models. Cell Rep. Methods *2*, 100297.

34. Beretta, S., Gritti, L., Ponzoni, L., Scalmani, P., Mantegazza, M., Sala, M., Verpelli, C., and Sala, C. (2022). Rescuing epileptic and behavioral alterations in a Dravet syndrome mouse model by inhibiting eukaryotic elongation factor 2 kinase (eEF2K). Mol. Autism *13*, 1.

35. Steinhoff, B.J., Staack, A.M., and Hillenbrand, B.C. (2017). Randomized controlled antiepileptic drug trials miss almost all patients with ongoing seizures. Epilepsy Behav. *66*, 45–48.

36. Lopez-Santiago, L., and Isom, L.L. (2019). Dravet Syndrome: A Developmental and Epileptic Encephalopathy. Epilepsy Curr. *19*, 51–53.

37. Han, Z. (2020). Antisense oligonucleotides increase Scn1a expression and reduce seizures and SUDEP incidence in a mouse model of Dravet syndrome. Sci. Transl. Med. *12*, eaaz6100.

38. Colasante, G., Lignani, G., Brusco, S., Di Berardino, C., Carpenter, J., Giannelli, S., Valassina, N., Bido, S., Ricci, R., Castoldi, V., et al. (2020). dCas9-Based Scn1a Gene Activation Restores Inhibitory Interneuron Excitability and Attenuates Seizures in Dravet Syndrome Mice. Mol. Ther. *28*, 235–253.

39. Valassina, N., Brusco, S., Salamone, A., Serra, L., Luoni, M., Giannelli, S., Bido, S., Massimino, L., Ungaro, F., Mazzara, P.G., et al. (2022). Scn1a gene reactivation after symptom onset rescues pathological phenotypes in a mouse model of Dravet syndrome. Nat. Commun. *13*, 161.

40. Nelson, S.B., and Valakh, V. (2015). Excitatory/Inhibitory Balance and Circuit Homeostasis in Autism Spectrum Disorders. Neuron *87*, 684–698.

41. Brunklaus, A., Ellis, R., Reavey, E., Forbes, G.H., and Zuberi, S.M. (2012). Prognostic, clinical and demographic features in SCN1A mutation-positive Dravet syndrome. Brain *135*, 2329–2336.

42. Johnson, J.I., Kirsch, J.A., Reep, R.L., III, and Switzer, R.C., 3rd. (1994). Phylogeny through Brain Traits: More Characters for the Analysis of Mammalian Evolution. Brain Behav. Evol. *43*, 319–347.

43. Croxson, P.L., Forkel, S.J., Cerliani, L., and Thiebaut de Schotten, M. (2017). Structural Variability Across the Primate Brain: A Cross-Species Comparison. Cerebr. Cortex *28*, 3829–3841.

44. Chiaradia, I., and Lancaster, M.A. (2020). Brain organoids for the study of human neurobiology at the interface of in vitro and in vivo. Nat. Neurosci. *23*, 1496–1508.

45. Koh, B., Kim, Y.E., Park, S.B., Kim, S.S., Lee, J., Jo, J.H., Lee, K., Bae, D.H., Kim, T.Y., Cho, S.H., et al. (2024). Unraveling the Molecular Landscape of SCN1A Gene Knockout in Cerebral Organoids: A Multiomics Approach Utilizing Proteomics, Lipidomics, and Transcriptomics. ACS Omega *9*, 39804–39816. https://doi.org/10.1021/acsomega.4c05039.

46. Mariani, J., Coppola, G., Zhang, P., Abyzov, A., Provini, L., Tomasini, L., Amenduni, M., Szekely, A., Palejev, D., Wilson, M., et al. (2015). FOXG1-Dependent Dysregulation of GABA/Glutamate Neuron Differentiation in Autism Spectrum Disorders. Cell *162*, 375–390.

47. Reinhardt, P., Glatza, M., Hemmer, K., Tsytsyura, Y., Thiel, C.S., Höing, S., Moritz, S., Parga, J.A., Wagner, L., Bruder, J.M., et al. (2013). Derivation and Expansion Using Only Small Molecules of Human Neural Progenitors for Neurodegenerative Disease Modeling. PLoS One *8*, e59252.

48. Elkabetz, Y., Panagiotakos, G., Al Shamy, G., Socci, N.D., Tabar, V., and Studer, L. (2008). Human ES cell-derived neural rosettes reveal a functionally distinct early neural stem cell stage. Genes Dev. *22*, 152–165.

49. Wu, T., Hu, E., Xu, S., Chen, M., Guo, P., Dai, Z., Feng, T., Zhou, L., Tang, W., Zhan, L., et al. (2021). clusterProfiler 4.0: A universal enrichment tool for interpreting omics data. Innovation *2*, 100141.

50. Fernández-García, S., Orlandi, J.G., García-Díaz Barriga, G.A., Rodríguez, M.J., Masana, M., Soriano, J., and Alberch, J. (2020). Deficits in coordinated neuronal activity and network topology are striatal hallmarks in Huntington's disease. BMC Biol. *18*, 1–16.

51. Estévez-Priego, E., Moreno-Fina, M., Monni, E., Kokaia, Z., Soriano, J., and Tornero, D. (2023). Long-term calcium imaging reveals functional development in hiPSC-derived cultures comparable to human but not rat primary cultures. Stem Cell Rep. *18*, 205–219.

52. Montalà-Flaquer, M., López-León, C.F., Tornero, D., Houben, A.M., Fardet, T., Monceau, P., Bottani, S., and Soriano, J. (2022). Rich dynamics and functional organization on topographically designed neuronal networks in vitro. iScience *25*, 105680.

STAR★METHODS

KEY RESOURCES TABLE

REAGENT or RESOURCE	SOURCE	IDENTIFIER
Antibodies		
NeuN polyclonal	Novusbio	Cat# NBP1-77686, RRID:AB_11009597
Anti-TUBB3 (Tuj1) mouse	BioLegend	Cat# 801201; RRID:AB_2312773
Anti-GFAP, chicken	Merck	Cat# AB5541; RRID:AB_177521
Anti-GFAP, rabbit	Genetex	Cat# GTX108711; RRID:AB_2037091
Anti-MAP2, chicken	Abcam	Cat# ab5392; RRID:AB_2138153
Anti-Nestin, rabbit	Biolegend	Cat# 841901; RRID:AB_2565468
Anti-PAX6, rabbit	Genetex	Cat# GTX113241; RRID:AB_1951119
Anti-SOX2, rabbit	Invitrogen	Cat# 48-1400; RRID:AB_2533841
Anti-Pro-Caspase-3	Sigma	Cat# C8487; RRID:AB_476884
Anti-NFM, rabbit	Abclonal	Cat# A19085; RRID:AB_2862577
Anti-GABA, rabbit	Sigma	Cat# A2052; RRID:AB_477652
Anti-Syn1, rabbit	Novus Biological	Cat# NB300-744; RRID:AB_609271
Anti-NeuN, rabbit	Abcam	Cat# ab177487; RRID:AB_2532109
Anti-NFH, rabbit	Genetex	Cat# GTX110065; RRID:AB_1950985
Anti-GFP, mouse	Invitrogen	Cat# 11559046; RRID: N/A
Anti-GAD65, rabbit	Genetex	Cat# GTX133096; RRID:AB_2886823
Anti-SCN1A, rabbit	Abcam	Cat# ab24820; RRID:AB_448395
Anti-rabbit, Alexa Fluor 488, donkey	Thermo	Cat# A-21206; RRID:AB_2535792
Anti-mouse, Alexa Fluor 594, goat	Jackson	Cat# 715-585-150; RRID:AB_2340854
Anti-chicken Alexa Fluor 647, donkey	Jackson	Cat# 703-605-155; RRID:AB_2340379
Bacterial and virus strains		
AAV7m8 (pAAV.Syn.GCaMP6s.WPRE.SV40)	The AAV was generated by Viral Vector Production Unit UAB (https://viralvector.eu)	The backbone was obtained from Addgene (Cat#100843)
Second generation Venus reporter LV	The backbone was obtained from Elisa Espinet	N/A
Chemicals, peptides, and recombinant proteins		
Cellbrite Green	Biotium	Cat#30022
mTESR1	Stem Cells Technologies	Cat# 85850
Matrigel	Cultek	Cat# 45354277
BrainPhys Imaging Optimized Medium	Stem Cells Technologies	Cat# 05796
Dorsomorphin	Fisher	Cat# 16458367
SB43152	MedChemExpress	Cat# HY-10431
SAG	Stem Cells Technologies	Cat# 73412
IWR1	Sigma	Cat# 681669-10 MG
EGF	Peprotech	Cat# AF-100-15
bFGF	Life Technologies	Cat# 100-18B-10UG
VPA (Valproic Acid)	Quimigen	Cat# HY-10585
PHT (Phenytoin)	Sigma	Cat# 1535008
Lam (Lamotrigine)	Sigma	Cat# L3791-10 MG
CBD (Cannabidiol)	Sigma	Cat# C7515-25 MG
FFA (Fenfluramine)	Sigma	Cat# 2695-10 MG
Critical commercial assays		
RNeasy mini kit	Qiagen	Cat#74104
EnVision Flex kit	Agilent	Cat#GV80011-2

(*Continued on next page*)

Continued

REAGENT or RESOURCE	SOURCE	IDENTIFIER
Deposited data		
RNAseq fastq samples	This paper	GSE256142
Experimental models: Cell lines		
hESC H9	Wisconsin Cell	WA009 (H9)
CTL iPSC - CW70019	Fujifilm	CW70019
DS14 - PFIZi014-A	EBISC - EACC	PFIZi014-A
DS16 - PFIZi016-A	EBISC - EACC	PFIZi016-A
Software and algorithms		
Fiji	ImageJ	https://imagej.nih.gov/ij/
Rstudio	R 4.4.3	https://www.R-project.org/
Imaris	Oxford Instruments	https://imaris.oxinst.com/
HTSeq software	Python 3.0	https://doi.org/10.1093/bioinformatics/btac166
MultiQC	Python 3.0	https://doi.org/10.1093/bioinformatics/btw354
DESeq2	R 4.4.3	https://doi.org/10.1186/s13059-014-0550-8
ComBat	R 4.4.3	https://doi:10.18129/B9.bioc.sva
gseGO	clusterProfiler	https://10.1038/s41596-024-01020-z
NETCAL software	Netcal	http://www.itsnetcal.com/
SNT pluggin	Fiji	https://doi:10.1038/s41592-021-01105-7
skimage package	Python 3.0	http://scikit-image.org
Tensorflow library	Python 3.0	https://www.tensorflow.org/
SciPy	Python	https://doi:10.1038/s41592-019-0686-2
Other		
Zeiss LSM 880	Microscope	Zeiss LSM 880
Zeiss LSM 980 Airyscan2	Microscope	Zeiss LSM 980 Airyscan2
Zeiss Axio Imager M2 Apotome 3	Microscope	Zeiss Axio Imager M2 Apotome 3
Leica CM1860 UV cryostat	Cryostat	Leica CM1860 UV cryostat
Olympus IX70 fluorescence inverted microscope	Microscope	Olympus IX70 fluorescence inverted microscope
Fast Hamamatsu camera	Camera	Fast Hamamatsu camera

EXPERIMENTAL MODEL AND STUDY PARTICIPANT DETAILS

Brain organoids generation

Commercial embryonic stem cell line WA009 (H9), iPSC control (CW70019), and commercial iPSCs derived from Dravet Syndrome patients (Ref. PFIZi014-A, PFIZi016-A, EBISC) were cultured in mTESR1 (ref. 85850, Stem Cells Technologies) on 1:40 Matrigel (ref. 45354277, Cultek) until they reached 70–80% confluence in 6-well plate multiwell format. The human pluripotent stem cell lines used in this study include one blastocyst-derived embryonic stem cell line (H9) and three induced pluripotent stem cell (iPSC) lines reprogrammed from peripheral blood mononuclear cells (PBMCs) of donors aged 10–69 years. Specifically, two iPSC lines were derived from pediatric donors (ages 10–14 and 15–19) diagnosed with Dravet Syndrome. While we acknowledge that the inclusion of pediatric-derived iPSCs deviates from ISSCR's most recent recommendations favoring adult donor sources for organoid research, the choice was driven by the clinical relevance of modeling an early-onset genetic epileptic disorder. All cell lines were obtained from established repositories with appropriate consent and ethical approval. This study adheres to institutional and national ethical guidelines, and we explicitly note this deviation for transparency.

To generate the brain organoids following a previously published unguided brain organoids protocol Lancaster, 2014[8], cells were dissociated using Gentle Cell Dissociation Reagent (ref. 100–0485, Stem Cells Technologies)and plated in mTESR1 with Y27632 Rock Inhibitor (Ref. TO-1254-10 MG, Biogene) in 96 round bottom non-adherent cell culture plates (Ref. CLS7007-24 EA, Corning) at a density of 9000 cells per well. Once self-aggregated organoids reached a diameter of 500–600 μm, approximately on day four of

differentiation, they were switched to neural induction medium, as in Lancaster, 2014.[9] Upon the formation of the neuroepithelium, which is visible at approximately day 8–10 depending on the iPSC line, the organoids were embedded in a Matrigel droplet and transferred to non-treated 6 mm plates with cerebral organoid differentiation medium without vitamin A. The neuroepithelial buds were allowed to expand in this medium for four days under static culture conditions. After four days, the embedded organoids were transferred to orbital agitation with Vitamin A supplemented cerebral organoid differentiation medium for further maturation, as described in Lancaster et al. 2014.[9] Brain organoids were matured on agitation (70rpm) for 90 days at 37°C and 95% humidity, with partial media replacement twice a week.

2D neuronal cultures preparation

Briefly, we adapted the protocols described by Reinhardt et al. 2013[47] and Elkabetz et al. 2008[48] to derive from the stem cells a neuronal culture enriched in inhibitory populations. To initiate neural induction of the EBs, bone morphogenic protein (BMP) inhibitor dorsomorphin (DM) ref. 16458367, Fisher) and transforming growth factor β (TGFβ)-signaling inhibitor SB43152 (Ref. HY-10431 5 mg, MedChemExpress) were supplemented to the basic induction media (DMEM/F12 supplemented with N2, Glutamine and NEAA, ref. 11330057; 17502048; 35050061 and 17504044; Life Technologies). To parallelly induce the ventral fate of the NPCs, SAG (Smoothened Agonist, an SHH pathway activator; ref. 73412, StemCell) and IWR-1 (a Wnt pathway inhibitor; ref. 681669-10 MG, Sigma.) were added to the induction media during the first 7 days. Once the neuroepithelia was clearly visible, neurospheres were transferred to Matrigel coated plates in NPC basic medium (50–50% DMEM/F12 - Neurobasal medium supplemented with 2% of B27 -vitA (ref. 12587010, Life Technologies) 1% of *N*-2, 1% Glutamax (ref. 35050-038, Gibco), 0.5% NEAA (ref. 11140050, Life Technologies), 20 ng/mL of Epidermal Growth Factor (EGF; Ref. AF-100-15, Peprotech) and bFGF 20 ng/mL (ref. 100-18B-10UG, Life Technologies) during 10 days. NPCs were then detached with trypsin and re-plated on Poly-ornitin/laminin (Ref. P4638-1G, Sigma; Ref. L2020-1 MG, Sigma) coated dishes for expansion during 3–4 passages. To differentiate NPCs toward neurons, cells were plated on Poly-ornitin/laminin coated dishes in the differentiation medium (50–50% DMEM/F12 - Neurobasal medium supplemented with 2% of B27, 1% of *N*-2, 1% Glutamax, 0.5% NEAA) for 4 weeks.

METHOD DETAILS

Immunofluorescence analysis

Cerebral organoids were fixed for 1 h at room temperature with 4% paraformaldehyde (PFA; ref. 141451.1211, Merck) and washed three times with 1x phosphate-buffered saline (PBS; ref. 21-040-CV, Corning) before overnight cryopreservation in 30% sucrose. After cryopreservation, organoids were embedded in OCT (ref. 05–9801, Bio-Optika), and cryosectioned at 10 μm-thick slices using a Leica CM1860 UV cryostat. For immunostaining, sections were Blocked/permeabilized in buffer solution containing 3% donkey serum (Ref. D9663, Merck), 2% bovine serum albumin (BSA) (Ref. A2153, Merck) and 0.1% Triton X-100 (Ref. X100, Merck) in 1x PBS for 1 h at room temperature. Subsequently, sections were incubated overnight with primary antibodies at 4°C (See key resources table for details). Sections were washed twice 1x PBS containing 0.1% Triton X-100 (PBS-T), stained with secondary antibodies, washed 3x in PBS-T and labeled with DAPI for nuclear counterstaining. Slides were mounted in Mowiol 4–88 (ref. 31381, Merck). Imaging was performed using Zeiss LSM 880, Zeiss LSM 980 Airyscan2 inverted confocal microscopes, or Zeiss Axio Imager M2 Apotome 3. For image processing and quantification, FIJI (ImageJ) was used. Brightness was adjusted for each maximal projection individually according to z stack volume. Quantifications were performed using Fiji's Analyze functions: particles tool involved manual intensity correction before binary conversion and Watershed segmentation. Size and circularity parameters were adjusted depending on the image magnification and the nature of the staining (nuclear or cytoplasmic). 3D viewer (Imaris) was used to record the video shown in Video S1.

For CellBrite IF co-staining, the protocol was adjusted to achieve low permeabilization in order to preserve the CellBrite staining. Briefly, the Triton concentration in the blocking solution was reduced to 0.01%. Diluted CellBrite was incubated during 10 min prior to nuclear staining with DAPI.

RNA preparation

Brain organoids were harvested and snap-frozen in liquid nitrogen and stored at −80°C upon their processing. RNA extraction was performed as follows: mechanic homogeneization in 700 μL Qiazol (ref. 15522515, Qiagen), phase separation in 140 μL Chloroform (Ref. C2432, Merck) followed by 15 min centrigution at 12000rpm; precipitation in Isopropanol (ref. 19516, Merck) and rehydration in 70%, final dilution in 100 μL of ultraPure water. Next, a column purification with the RNeasy Miki Kit (ref. 74104, Qiagen) was performed following the supplier protocol. QC was validated in a Bioanalyzer.

For each condition, the following experimental approach was determined: CTL day 21 (2 replicates; 6 organoids per replicate), day 35 (2 replicates, 4 organoids per replicate), and day 90 (2 replicates, 2 organoids per replicate); iPSC DS (DS14 and DS16) and control (H9 and CTL 70019) day 35 and day 90 (2 replicates, 2 organoids per replicate); and day 90 organoids after VPA treatment from both control and DS lines (2 replicates, 2 organoids per replicate).

RNAseq analysis

RNA sequencing was conducted at the Universitat Pompeu Fabra (UPF) Genomics Service and BGITech Global RNAseq libraries were prepared using polyA capture and QC validated in Bioanalyzer. Libraries were pooled together, and sequenced on a

NexSeq 500, using a 2x75 cycles High Output run, in addition to a 2x75 cycles Mid Output run. Transcript alignment was performed on STAR software was utilized against the human reference GRCh38 and annotation version 109 from Ensembl. Counts were obtained using HTSeq software, and MultiQC software was employed for quality assessment. The count matrices were fed into the DESeq2 statistical package (R) to determine differential transcript expression between samples, employing adjusted *p*-value and lfcThreshold parameters of 0.05 and 0.58, respectively. Principal component analysis (PCA) was conducted after batch correction (ComBat), illustrating the variance between distinct sample groups and the similarity within sample replicates. Distance heatmap was generated to display the large distance between time points and the tight clustering within the same replicates. For the visualization of heatmaps and other visual representations derived from the analysis of differential expression, ggplot was implemented. To conduct the Gene Set Enrichment Analysis of Gene Ontology, the gseGO function from clusterProfiler[49] was employed.

Histological staining

For hematoxylin/eosin (H/E) staining, fixed and cryosectioned samples were subjected to hematoxylin staining, which was carried out for 5–10 min. To enhance nuclear contrast, the slides were submerged in water for 5 min before incubating with eosin staining for 1 min to highlight cytoplasmic structures. Finally, the samples were mounted for microscopic examination. For inmunohistochemistry, EnVision Flex kit (Ref. GV80011-2, Agilent) was used through DAKO Autostainer. Briefly, fixed and cryosectioned samples were incubated in antigen retrieval solution (EnV FLEX TRS, High pH) for 30 min at 97°C prior to 20 min incubation with primary antibody (NeuN polyclonal, Novusbio). After, the sections were washed, incubated with the blocking solution (EnV FLEX PeroxidaseBlocking Reagent) for 3 min and finally incubated with an HRP conjugated secondary antibody (EnV FLEX/HRP) for 20 min.

Intracellular calcium recording analysis

Live calcium imaging was performed in 7 control (H9 hESC and CTL lines) and 8 Dravet (DS16 and DS14 iPSC lines) brain organoids at day 100–180 of differentiation using the GCaMP6s calcium indicator. GCaMP6s was expressed in neurons using AAV7m8-SYNI-GCaMP6s. For the infection, organoids were transferred into a 48WP. For 4 organoids, 2.5 μL of the virus was diluted in 400 μL of differentiation media. The day after, 400 μL of differentiation media was added to each well. After that, half of the media was changed twice a week as usual. Intracellular calcium imaging was performed in an Olympus IX70 fluorescence inverted microscope equipped with a fast Hamamatsu camera using 10x objective and 33 frames per second. Several regions of each organoid were recorded during 11 min at days 7, 11 and 14 after infection in BrainPhys media. Recorded movies of intracellular calcium fluorescence were analyzed using NETCAL software (www.itsnetcal.com)[50] in combination with other custom-made packages, providing the raster plots of spontaneous neuronal activity and connectivity matrices. Neural interactions and functional connectivity were captured using Global Efficiency and Community Statistic as previously described[51,52]

Low dosage viral infection

Second generation lentivirus production was performed by transient transfection of 293T cells with a packaging vector (psPAX2), an envelope vector (pMD2.G) and the lentiviral vector pV2luc2, which contains a Venus reporter cassete under the control of an ubiquitous promoter. After 48 and 72 h of transfection, supernatants containing viral particles were collected, pooled, and rapidly frozen at −80°C for storage.

90 days-old brain organoids were transduced using 1:5 and 1:20 diluted supernatant in maturation media. After a 24-h infection period, brain organoids were washed and supplied with fresh maturation media. 3D viewer (Imaris) was used to record the video shown in Video S2. SNT pluggin from FIJI was used for the segmentation of images shown in Figure S4.

Live imaging

For live imaging, matured brain organoids at day 35 and day 90 were incubated with green Cellbrite (0.5 μL in 100 μL of media) dye for 1 h under agitation. Throughout the imaging process, the organoids were kept in BrainPhys Imaging Optimized Medium. Wide-field imaging was performed using a Zeiss Axio Observer Z1 microscope with a 10x objective and stitching option (10% overlap). Images were captured in a z stack with 50 μm intervals for a 500 μm. The stitched images, containing each the whole z stack depth, were then exported in.czi format, and the separated tiles were saved in.tiff format for subsequent analysis.

For viral transduced neuronal tracing, organoids were transferred to a 24-well iBIDI plate with BrainPhys media (ref. 05796, StemCell) and subjected to imaging using a Confocal Carl Zeiss LSM 880 at 37°C with CO_2 settings. Images were captured at 25x magnification with oil immersion.

Drug testing experiment

Ninety-days old organoids were accutely treated for one week with antiseizure drugs, including Valproic Acid, Phenytoin, Lamotrigine, Cannabidiol, and Fenfluramine. Briefly, three organoids per well were plated into a 24-well plates (ref. 142485, DDBiolab), and treated with the anti-seizures drugs (final concentration: VPA-1mM (Ref. HY-10585, Quimigen), PHT-1mM (ref. 1535008, Sigma), Lam-200μM (Ref. L3791-10 MG, Sigma), CBD-10μM (Ref. C7515-25 MG, Sigma), and Fenfluramine-10μM (2695-10 MG, Sigma)). Half-volume medium change, maintaining drug concentration, was performed on day three.

For live-imaging, organoids were stained with Cellbrite Green (ref. 30022, Biotium) 0.5 μL in 100 μL of media) dye for 1 h under agitation, and imaging was performed before starting the treatment and after 7 days, prior to fixation.

Image preprocessing

All the images from the dataset have been preprocessed before using them to train the DCNN following the steps below described. Focus stacking (1): to generate a suitable 2D projection for each stack of images representing the same x and y pixels but at different depth we have implemented an algorithm based on the Laplacian of Gaussian (LoG). This algorithm has been implemented using the Laplace and Gaussian filter offered by the skimage package in Python with a $\sigma = 2$ and a kernel size of 10 for the Gaussian filter and a kernel size of 10 for the Laplacian filter. Since the regions on focus are regions of rapid intensity change, the pixels in these regions will get large LoG scores. Nevertheless, the regions out-of-focus are blurry and the pixels in these regions will get low LoG scores. Therefore only the intensity value at the stack where the LoG (x, y, z) achieves maximum is retained. Image intensity correction (2): minimum and maximum intensity values from all the tiles representing the same organoid are considered to homogenize the intensity of the different images by applying a first normalization step. Then, pixels with an intensity value over 25 are selected to define the organoid region. Those below the threshold are considered as background. Intensity gamma correction according to the mean intensity value of the organoid region is applied to the image in order to homogenize the intensity among tiles (the gamma values used for the correction are 0.6 if the mean intensity value is bellow 25, 0.8 if the mean intensity value was between 25 and 65, 1 if the mean intensity value was over 65). Image stitching (3): ImageJ plugin Grid/Collection Stitching is used to stitch the different tiles and generate a single 2D image. Phase correlation and fast Fourier Transform were applied to find the correct overlap of connected tiles, and linear blending fusion algorithm was used to ensemble the different tilesin a single image. Image fragmentation (4): A window filter of 224x224 with a stride of 224 was used to fragment each pre-processed image. Fragments with at least 90% of pixels over the intensity threshold (>35) were selected and included in the dataset. Data clearing (5): Finally, manual filtering is performed to remove non-QC images Filtering parameters include: images of the external part of the organoid containing allos, artifacts caused by image reconstruction process, blurred images or background images not discarded in the previous step. In d0 we started with 3160 images and we ended with 1619 images 1541 images were discarded.

ImPheNet: Dataset generation

For phenotype prediction, we generated a dataset containing CTL (iPSC CTL and hESC H9) and DS (DS14 and DS16) images acquired from 90 days-old brain organoids after 1h of Cellbrite incubation (from a total of 100 organoids). To develop the model only DS14 and H9 were used and number of images selected were 819 for DS14 and 800 for h9. So, the ratio was close to 1:1. Indeed, the amount of organoids was 27 for h9 and 28 for DS.

A second dataset for drug testing organoids was created with the following categories: treated (INH) and untreated DS (DS14 and DS16) 7 days after Cellbrite incubation. CORIs derived from the same organoid were labeled with the same ID and allocated to the same subset of data (training-validation-test).

In both cases, 75% of CORIs were used for training the model (incluing 25% for model validation) and 25% for testing. Stratified splitting based on organoid ID ensured that each subset kept the same proportion of classes as in the original dataset. However, since not all the organoids contain the same amount of CORIs the proportionality between classes is just partially respected. Data augmentation based on image rotations and image flips was implemented in an online approach to enlarge the dataset. Intensity distribution in each CORIs was corrected using the gamma correction factor (based on mean intensity). Finally, a normalization step based on histogram stretching was applied to ensure that all the images are defined by the same range of intensity values (from 0 to 1).

ImPheNet: DL model

Two different DL models were trained considering the question to address: one for genotype prediction (identification of organoid genotype through its phenotype) (1) and another for drug testing (Identification of organoids treated with sodium channel inhibitory drugs) (2). The output value from the first FL model is the probability of a particular region of being control (1), And from the second DL model the probability of a particular region of being affected by a sodium channel inhibitory drug (2). Both models were generated by transfer learning from pretrained models available in Python Tensorflow library, after exploring the space of hyperparameters. Each final model was selected according to validation accuracy (the highest the best) and validation loss (the lowest the best). For each model, all the metrics (accuracy, jaccard similarity, dice similarity, sensitivity, and specificity) were calculated using the SciPy python package considering each sample independently. For detailed information about the model see Table S4.

ImPheNet: DL model results

The binary outputs of the DL models were ensembled into a simple score classification using a simple mathematical computation. First, all the CORIs predictions from the same organoid were joined in a vector that was then split in two considering the value of the predictions: predictions below and above a given threshold.The threshold was settled using the validation subset and selecting the value which maximazes the validation accuracy. Then, all the predictions were scaled from 0 to 1 to get the class intensity of all the samples in the same scale (Equation 1). This is necessary in case the threshold is not 0.5. Then, the mean intensity per class is obtained and the class score is computed as in Equation 2.

$$scaled_org_preds_bellow_th = \frac{th - org_{preds_{below_{th}}}}{th}$$
$$scaled_org_preds_over_th = \frac{org_preds_over_th - th}{1 - th} \quad \text{(Equation 1)}$$

$$class_0_score = \frac{class_0_mean_intensity * n_preds_below_th}{len(org_preds)}$$
$$class_1_score = \frac{class_1_mean_intensity * n_preds_over_th}{len(org_preds)} \quad \text{(Equation 2)}$$

As a result of the scoring, we generated two statistics. In the case of the phenotype DL model, class 0 corresponds to DS and class 1 to CTL. In the case of the drug testing DL model, class 0 corresponds to DS organoids in control conditions (non-treated) while class 1 corresponds to DS organoid treated with a sodium channel inhibitory drug. Given the heterogeneity in the number of CORIs per organoid, to compare the results coming from organoids with different number of samples we used a normalized histogram with 20 bins. Each normalized histogram of 20 bins was created counting the number of predictions comprised in each region of the probability range (0–1 divided in 20).

QUANTIFICATION AND STATISTICAL ANALYSIS

Quantification methods are described above. Statistical analyses were performed in R. The statistical test used and the definition of statistical significance in each case is included in the figure legends.